Cell Reports

Article

The Protein Arginine Methyltransferase PRMT8 and Substrate G3BP1 Control Rac1-PAK1 Signaling and Actin Cytoskeleton for Dendritic Spine Maturation

Graphical Abstract

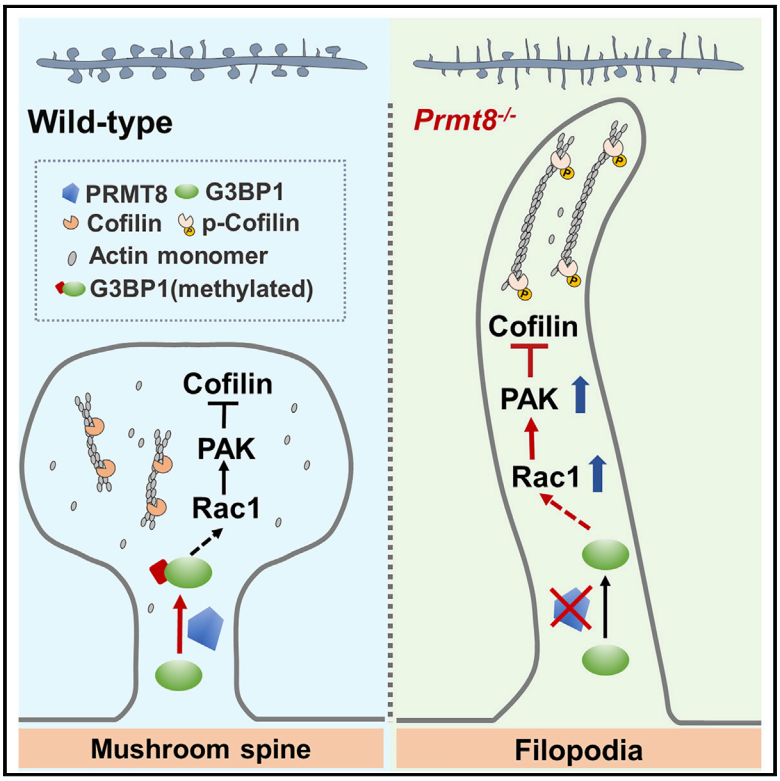

Highlights

- PRMT8 is upregulated in hippocampus during dendritic spine maturation
- Depletion of PRMT8 generates more filopodia
- Lack of PRMT8 increases cofilin phosphorylation and slows actin turnover
- Spine maturation depends on arginine methylation of the PRMT8 substrate G3BP1

Authors

Louisa Hoi-Ying Lo, Rui Dong, Quanwei Lyu, Kwok-On Lai

Correspondence

laiko@hku.hk

In Brief

Lo et al. demonstrate that PRMT8 is localized at neuronal synapses and methylates the dendritic RNA-binding protein G3BP1. This promotes synapse maturation by regulating Rac1 and synaptic actin dynamics. Therefore, arginine methylation, a well-known protein modification in the nucleus, also acts in dendrites to control neuronal development.

Lo et al., 2020, Cell Reports *31*, 107744
June 9, 2020
https://doi.org/10.1016/j.celrep.2020.107744

CellPress

Cell Reports

CellPress
OPEN ACCESS

Article

The Protein Arginine Methyltransferase PRMT8 and Substrate G3BP1 Control Rac1-PAK1 Signaling and Actin Cytoskeleton for Dendritic Spine Maturation

Louisa Hoi-Ying Lo,[1,3] Rui Dong,[1,3] Quanwei Lyu,[1] and Kwok-On Lai[1,2,4,*]
[1]School of Biomedical Sciences, The University of Hong Kong, Hong Kong, China
[2]State Key Laboratory of Brain and Cognitive Sciences, The University of Hong Kong, Hong Kong, China
[3]These authors contributed equally
[4]Lead Contact
*Correspondence: laiko@hku.hk
https://doi.org/10.1016/j.celrep.2020.107744

SUMMARY

Excitatory synapses of neurons are located on dendritic spines. Spine maturation is essential for the stability of synapses and memory consolidation, and overproduction of the immature filopodia is associated with brain disorders. The structure and function of synapses can be modulated by protein post-translational modification (PTM). Arginine methylation is a major PTM that regulates chromatin structure, transcription, and splicing within the nucleus. Here we find that the protein arginine methyltransferase PRMT8 is present at neuronal synapses and its expression is upregulated in the hippocampus when dendritic spine maturation occurs. Depletion of PRMT8 leads to overabundance of filopodia and mis-localization of excitatory synapses. Mechanistically, PRMT8 promotes dendritic spine morphology through methylation of the dendritic RNA-binding protein G3BP1 and suppression of the Rac1-PAK1 signaling pathway to control synaptic actin dynamics. Our findings unravel arginine methylation as a crucial regulatory mechanism for actin cytoskeleton during synapse development.

INTRODUCTION

Dendritic spines are protrusions on dendrites that receive the most excitatory inputs from axons (Nimchinsky et al., 2002). Dendritic spines are heterogeneous in morphologies, with the mature mushroom spines possessing a bulbous spine head isolated from the dendritic shaft by a short neck. Mushroom spines are prominent in adult brain, whereas the long filopodia, which are abundant during early development, may act as spine precursors to initiate synaptogenesis (Ziv and Smith, 1996; McKinney, 2010). The maturation of mushroom spines along development is essential for proper functioning of synapses in terms of structural stability, signal transduction, and size of the postsynaptic density (Yuste, 2011). Dendritic spines are rich-in filamentous actin (F-actin), and the concerted actions of multiple actin-binding proteins such as nucleation factors, capping proteins, molecular motors, and depolymerization factors determine spine morphology and synaptic function (Hotulainen et al., 2009; Hotulainen and Hoogenraad, 2010; Korobova and Svitkina, 2010; Rex et al., 2010; Spence et al., 2016). Consequently, abnormal actin stabilization is observed in different mouse models of neurodevelopmental disorders that may alter spine morphology and lead to overabundance of filopodia (Chen et al., 2010; Baudry et al., 2012; Duffney et al., 2015; Yan et al., 2016; Pyronneau et al., 2017; Santini et al., 2017). Nonetheless, diverse pathways control actin dynamics in neurons, and it is likely that many key signaling proteins that converge on actin cytoskeleton and regulate spine maturation have yet to be identified.

Spine maturation depends on local dendritic protein synthesis (Lai and Ip, 2013). mRNA localization and translational regulation require specific RNA-binding proteins (RBPs), and their deficiency in neurons often leads to an increased number of filopodia (Goetze et al., 2006; Dictenberg et al., 2008; Muddashetty et al., 2011). For example, in fragile X syndrome, lack of the RBP fragile X mental retardation protein (FMRP) results in more filopodia and longer spines (Irwin et al., 2000; Fortin et al., 2012; Penzes et al., 2011; Phillips and Pozzo-Miller, 2015). Actin dynamics during synaptic plasticity are also impaired in *Fmr1* knockout neurons (Chen et al., 2010). Local translation may alter actin cytoskeleton directly through the synthesis of actin-binding proteins and their upstream regulators (Kashima et al., 2016; Michaelsen-Preusse et al., 2016; Feuge et al., 2019). Intriguingly, the two processes of protein synthesis and actin polymerization may also be interconnected indirectly through the translation initiation protein eIF4E and the FMRP-interacting protein CYFIP1 (De Rubeis et al., 2013). In the absence of FMRP, a shift in equilibrium of CYFIP1 between the translation initiation complex and the wave-regulatory complex (WRC) will hyperactivate the small guanosine triphosphatase (GTPase) Rac1 and its downstream targets PAK1 and LIM kinase, which inhibit the actin depolymerization factor cofilin through phosphorylation. The resulting stabilization of F-actin can generate more filopodia and immature spines

(Pyronneau et al., 2017; Santini et al., 2017; Hotulainen et al., 2009). It is not clear whether other dendritically localized RBPs similarly control synaptic actin cytoskeleton and spine morphogenesis through the Rac1-PAK1 pathway.

Given the major contribution of local mRNA translation to the dendrite-localized proteome (Zappulo et al., 2017), we reason that novel regulatory mechanisms of dendritic spine maturation may be identified by characterizing proteins encoded by dendritic mRNAs. High-throughput transcriptomic study has identified more than 2,000 transcripts in the hippocampal neuropil (Cajigas et al., 2012). Our data mining uncovers many unexpected candidates, including those that encode protein arginine methyltransferases (PRMTs). PRMT is a family of enzymes that catalyze the addition of the methyl group to arginine residue of the substrate. The role of PRMT-mediated arginine methylation in regulating gene transcription, RNA splicing, and nuclear export within the nucleus is well documented (Iberg et al., 2008; Cheng et al., 2007; Deng et al., 2010), but the importance of cytoplasmic PRMTs is less characterized. Among all nine PRMTs in mammal, PRMT8 is particularly interesting because its expression is largely restricted in the brain and is the only membrane-bound PRMT via N-terminal myristoylation (Lee et al., 2005; Sayegh et al., 2007). PRMT8 also possesses the unusual property of acting as both a methyltransferase and a phospholipase. Its phospholipase activity hydrolyzes phosphatidylcholine to regulate dendritic morphology and motor-coordinating behaviors (Kim et al., 2015). PRMT8 is required for synaptic plasticity in the hippocampus and memory formation (Penney et al., 2017). However, how PRMT8 regulates synaptic structure and function at the cellular level remains unknown.

Here we found that PRMT8 expression is increased in the hippocampus during spine maturation, and depletion of PRMT8 impairs spine maturation and alters actin dynamics because of hyperactivity of Rac1 and PAK1. These phenotypes are mimicked by depletion of G3BP1, a dendritic RBP whose function in spine maturation depends on PRMT8-mediated methylation and PAK1. Our findings have uncovered a previously uncharacterized function of arginine methylation outside the nucleus in regulating actin cytoskeleton and synapse maturation of neurons.

RESULTS

PRMT8 Is Present at Excitatory Synapses, and Its Expression Coincides with Spine Maturation

To understand the function of PRMT8 in hippocampal neurons, we first examined the subcellular location of *Prmt8* mRNA and protein. Discrete *Prmt8* mRNA puncta were detected in both cell soma and dendrites of hippocampal neurons (Figure 1A). About 8.8% of the dendritic *Prmt8* mRNA puncta were localized at distal dendrites 70–120 μm from the cell body (102 *Prmt8* mRNA puncta were quantified from 10 dendrites of 10 neurons). The puncta were absent when hybridized with the sense probe, indicating specificity of the *in situ* hybridization signals.

PRMT8 protein was also present in the synapse-enriched synaptoneurosome (SNS) fraction from the forebrain. Among other PRMTs examined, only PRMT4 and PRMT5 showed considerable expression in the SNS (Figure 1B). Immunostaining revealed that PRMT8 existed as distinct puncta on dendrites and some PRMT8 puncta were partially overlapped with the postsynaptic protein PSD-95 (Figure 1C) (29.4% ± 2.6% of PSD-95 puncta showed overlap with PRMT8 puncta, and 27.1% ± 2.5% of PRMT8 puncta showed overlap with PSD-95 puncta; mean ± SEM; 859 PSD-95 puncta and 933 PRMT8 puncta from 6 dendrites were analyzed; Pearson's coefficient 0.536 ± 0.016). GFP-tagged PRMT8 expressed in hippocampal neurons also appeared as discrete puncta along dendrites, and ~41% of the puncta were present in dendritic spine heads (Figure 1D) (338 puncta were analyzed from 6 dendrites).

PRMT8 is highly expressed in the human brain (Lee et al., 2005), but how the expression is regulated temporally has not been determined. We found that PRMT8 protein expression in the hippocampus was developmentally regulated: its expression was increased in hippocampal neurons upon maturation from 3 to 21 days *in vitro* (DIV) (Figure 1E). Interestingly, PRMT8 expression requires spontaneous neuronal activity, because the level was significantly reduced by the blockade of action potential with tetrodotoxin (Figure 1F). PRMT8 expression was also upregulated along development in the hippocampus *in vivo*, with a notable increase from postnatal day (P) 7 to P14 and a peak at P21 (Figure 1G). In the hippocampus, spine maturation begins between P6 and P12, during which the abundance of filopodia declines (Fiala et al., 1998). Filopodia in cultured hippocampal neurons are also reduced between the first and the second week *in vitro* (Papa et al., 1995). The precise development and behavior of dendritic spines in hippocampal neurons are not the same *in vitro* and *in vivo* (Harris et al., 1992; Papa et al., 1995; Segal, 2001; Ebrahimi and Okabe, 2014), which might account for the difference in temporal profiles of PRMT8 expression between the cultured neurons and the hippocampus. Nonetheless, the temporal regulation of PRMT8 expression and its localization at postsynaptic sites suggest PRMT8 might play a role in dendritic spine maturation.

PRMT8 Regulates Dendritic Spine Maturation through Protein Arginine Methylation

To address whether PRMT8 is crucial for spine maturation, two short hairpin RNAs (shRNAs) targeting rat PRMT8 were generated. Knockdown efficiency was examined by introducing the shRNAs into primary cortical neurons using nucleofection, followed by western blot (Figure 2A). Of the two shRNAs, shRNA-1028 was more efficient in repressing the level of PRMT8 and was used in subsequent experiments. The PRMT8 shRNA or control shRNA was cotransfected with the GFP construct into the primary hippocampal neuron in the presence or absence of the RNAi-resistant PRMT8 construct, and the densities of different spine types were analyzed. Introduction of the PRMT8-shRNA significantly reduced the density of mushroom spines and increased the density of filopodia. Importantly, both the loss of mushroom spines and the induction of filopodia were reversed by coexpression of PRMT8 (Figure 2B), indicating that the spine defects resulted from PRMT8 deficiency.

Protein arginine methylation is a major regulatory mechanism in the nucleus. However, the PRMT8-GFP expressed in neurons was not enriched in the nucleus but was more abundant in the cytoplasm and plasma membrane (Figure S1A), which is

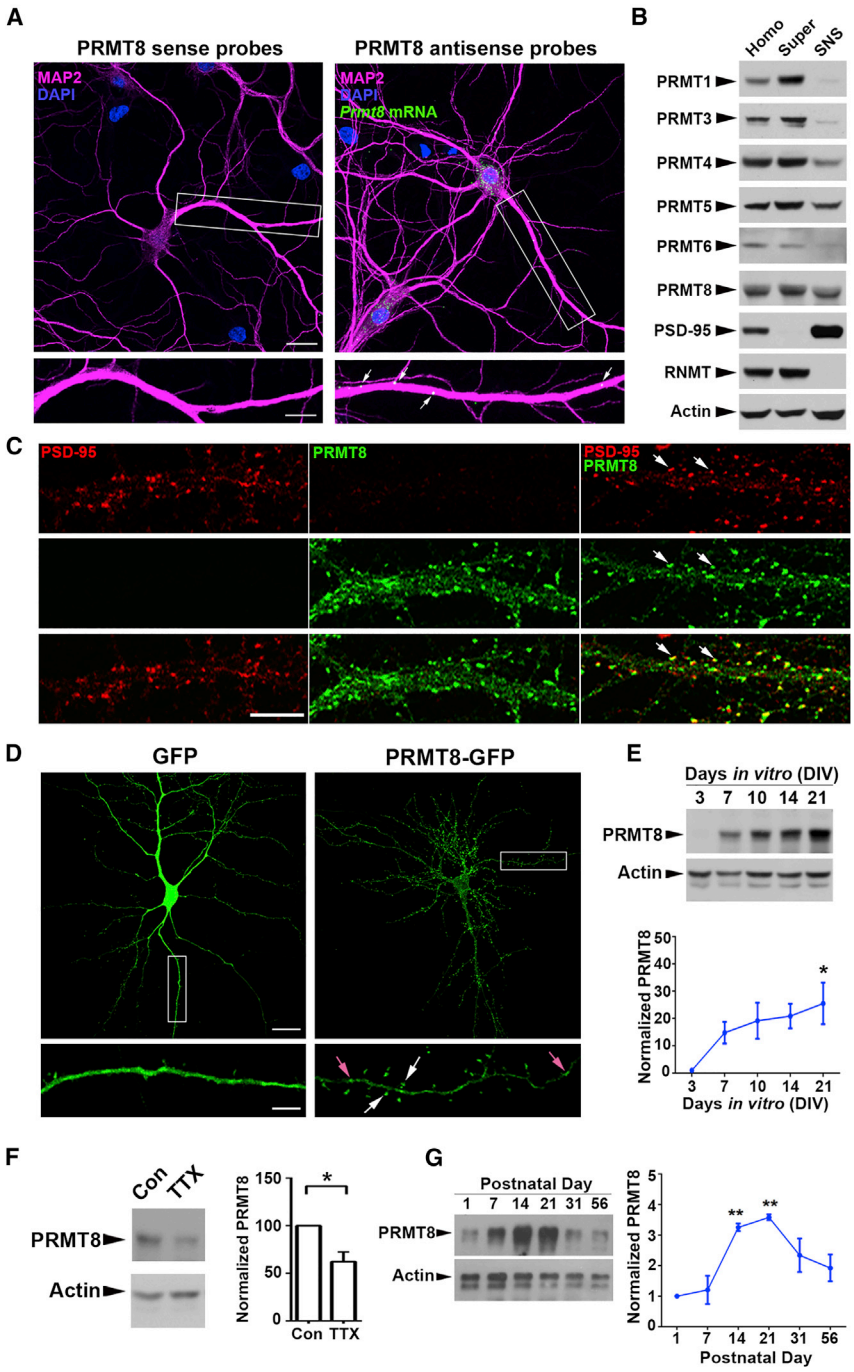

Figure 1. PRMT8 Is Synaptically Localized and Upregulated during Dendritic Spine Maturation

(A) *In situ* hybridization of rat hippocampal neurons (17 DIV), followed by staining of MAP2 (magenta) and nuclear marker DAPI (blue). *Prmt8* mRNA puncta (green, arrows) were found in dendrites. Scale bars: 20 μm (upper) or 10 μm (lower).

(B) Expression of various PRMTs in SNS, homogenate (Homo), and supernatant (Super).

(C) Immunofluorescence staining of PRMT8 protein (green) and PSD-95 (red) in primary hippocampal neurons (0.4×10^5 cells per 18 mm coverslip, 23 DIV). The PRMT8 (green) puncta were absent from the negative control lacking PRMT8 antibody (top row, middle panel), whereas the PSD-95 (red) puncta were absent from the control lacking PSD-95 antibody (middle row, left panel), indicating specificity of the signals. Examples of overlapped PRMT8 and PSD-95 puncta are indicated (arrows). Scale bar: 10 μm.

(D) Hippocampal neurons (1.4×10^5 cells per 18 mm coverslip) transfected with GFP-tagged PRMT8 or GFP, followed by staining with GFP antibody at 19 DIV. PRMT8 appeared as discrete puncta in the dendrite (pink arrows), and some were localized in the dendritic spine heads (white arrows). Scale bars: 20 μm (upper) or 5 μm (lower).

(E) Expression of PRMT8 in hippocampal neurons cultured for different durations as indicated. The intensity of PRMT8 was normalized with that of actin. Results were pooled from three independent experiments. Data were mean ± SEM; *$p < 0.05$ for the comparison between 3 and 21 DIV; one-way ANOVA, Tukey's multiple comparison test.

(F) Dissociated hippocampal neurons were treated with vehicle (Con) or TTX (2 μM) for 48 h. Results were pooled from four independent experiments. Data were mean ± SEM; *$p < 0.05$; Student's t test.

(G) Expression of PRMT8 was upregulated in the hippocampus at different developmental stages after birth. Results were pooled from three independent experiments. Data were mean ± SEM; **$p < 0.01$ for the comparison between P1 and P14 or P1 and P21; one-way ANOVA, Tukey's multiple comparison test.

consistent with a previous study showing a low level of PRMT8 in the nuclear fraction (Penney et al., 2017). To address whether PRMT8 function in spine maturation depends entirely on its action in the nucleus, we generated an RNAi-resistant PRMT8 variant through the addition of a nuclear localization signal (NLS) and the substitution of the second Gly to Ala to disrupt its membrane anchorage (Park et al., 2019). The PRMT8 variant was restricted in the nucleus (Figure S1B), and coexpression of this nuclear PRMT8 failed to rescue the reduction of mushroom spines and increase in filopodia after PRMT8 knockdown (Figure 2C). Overexpression of the nuclear PRMT8 by itself did not affect the density of mushroom spines or filopodia (Figure S1C), ruling out the possibility that expression of the nuclear PRMT8 may have an adverse effect on neurons. Therefore, a non-nuclear role of PRMT8 should be involved in spine maturation.

PRMT8 possesses both methyltransferase and phospholipase D catalytic activities (Kim et al., 2015). To distinguish which enzymatic activity is required for dendritic spine maturation, PRMT8 mutant constructs were created to disrupt either the methyltransferase (G121A) or the phospholipase D (K107R) activity (Figure S2). The loss of mushroom spines and overproduction

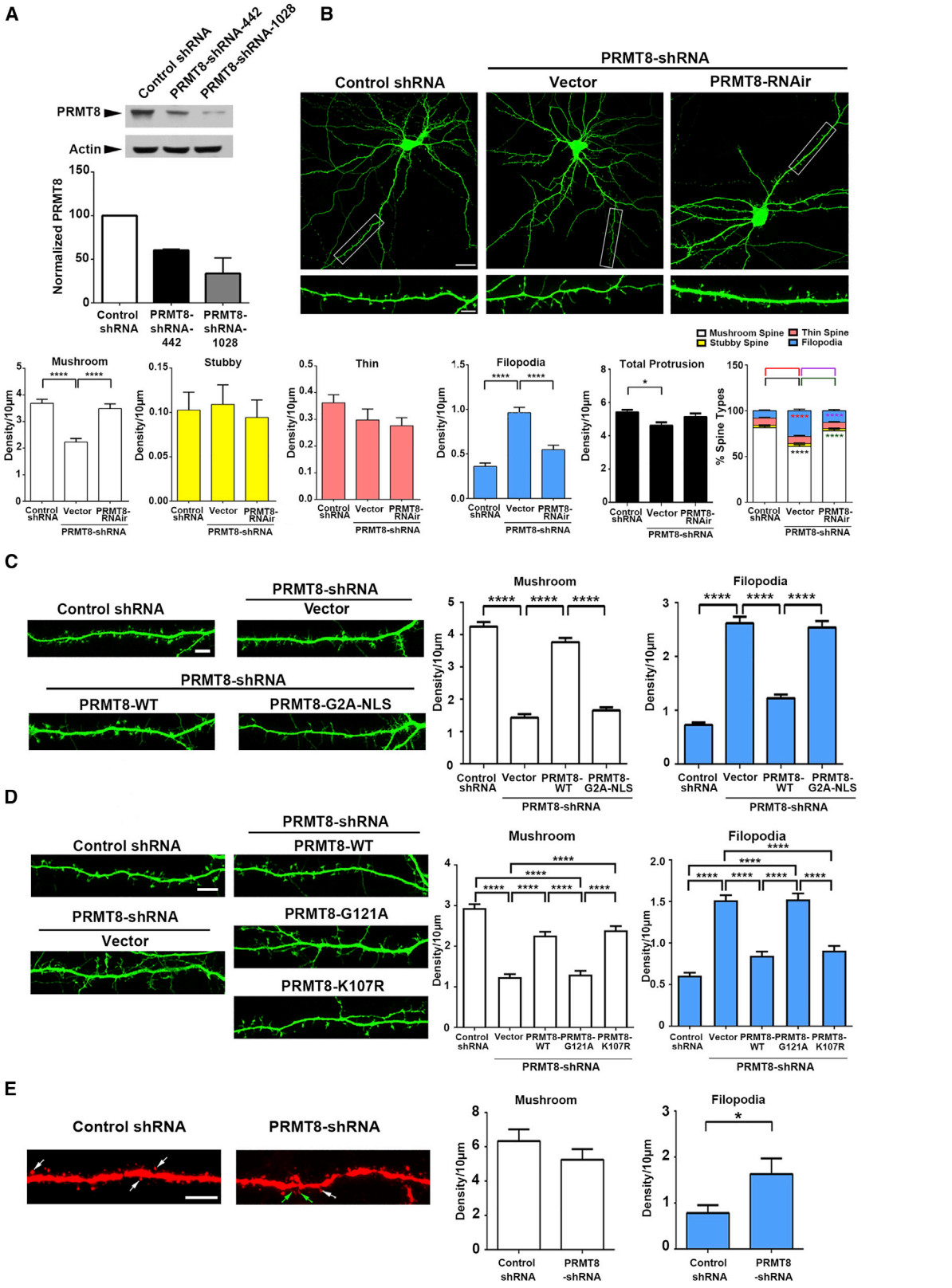

(legend on next page)

of filopodia induced by PRMT8-shRNA could only be rescued by the phospholipase-deficient K107R mutant, not the methyltransferase-deficient G121A mutant (Figure 2D). Therefore, PRMT8 promotes dendritic spine maturation mainly by catalyzing arginine methylation.

To investigate whether PRMT8 regulates spine maturation *in vivo*, control- or PRMT8-shRNA was introduced, together with tdTomato, into the ventricle of the mouse embryo by *in utero* electroporation. Dendritic spine morphology of the secondary apical dendrites of hippocampal CA1 neurons was examined at P21. Consistent with the altered spine morphology in primary neurons, PRMT8-shRNA significantly increased the density of immature filopodia (Figure 2E), indicating that PRMT8 regulates the maturation of dendritic spines *in vivo*.

PRMT8 Regulates Localization of Excitatory Synapses in the Dendritic Spines and Dendritic Shaft

To ask whether the spine defects upon PRMT8 knockdown are associated with a change in synapse number, patch-clamp recording was performed to measure the miniature excitatory postsynaptic current (mEPSC) (Figure 3A). Neither the mEPSC frequency nor its amplitude was significantly changed after PRMT8 knockdown (Figure 3B), suggesting that the number of excitatory synapses is not greatly affected despite the profound change in spine morphology.

During spine maturation, the disappearance of filopodia is accompanied by a decrease in the number of shaft synapses (Fiala et al., 1998). Therefore, delayed synapse maturation is characterized by more synapses being formed on the dendritic shaft (Yadav et al., 2017). To ask whether more shaft synapses are present after PRMT8 knockdown that can compensate for the loss of mushroom spines, primary hippocampal neurons were transfected with the calcium sensor GCaMP6. In the presence of tetrodotoxin (TTX), GCaMP6 will generate a fluorescence signal when calcium influx occurs through spontaneous NMDA receptor activation (Yadav et al., 2017). We found that the number of calcium transient events was reduced in the dendritic spines but increased in the dendritic shaft after PRMT8 knockdown, and this change was reversed by coexpression of PRMT8 (Figure 3C). Immunostaining of excitatory presynaptic protein vGLUT1 and postsynaptic PSD-95 confirmed the density of excitatory synapses was reduced in the dendritic spines but increased in the dendritic shaft upon PRMT8 knockdown, and the shift in synapse distribution was rescued by coexpression of PRMT8 (Figures 3D and 3E). Therefore, PRMT8 promotes synapse maturation by reducing the number of both filopodia and shaft synapses.

Impaired Spine Maturation and Altered Behavior in *Prmt8* Knockout Mice

If PRMT8 is essential for spine maturation, we anticipate that similar spine defects should be observed in neurons of *Prmt8* knockout mice. To test this hypothesis, primary hippocampal neurons were cultured from *Prmt8* knockout mice (*Prmt8*$^{tm1a(EUCOMM)Wsi}$) (Skarnes et al., 2011). PRMT8 expression was reduced by about 70% in heterozygous brain compared with wild-type control (+/+) and was absent from the homozygous knockout (Figure 4A). Consistent with the higher abundance of filopodia in PRMT8-shRNA-transfected neurons, the density of filopodia increased significantly in both heterozygous and homozygous *Prmt8* knockout neurons (Figures 4B and 4C). The number of mushroom spines tended to decrease in *Prmt8* knockout neurons, although the difference from wild-type control was not statistically significant (Figure 4C).

We also determined whether *Prmt8* knockout mice displayed abnormal spine morphology in the hippocampus *in vivo*. Spine morphology of secondary apical dendrites of hippocampal CA1 neurons was analyzed in 6-week-old mice. Although the densities of mushroom spines and filopodia were similar between wild-type and *Prmt8* homozygous knockout mice, the length of mushroom spines was significantly increased in the *Prmt8*-deficient neurons (Figure 4D).

Defective spine maturation is associated with abnormal behaviors such as impaired sociability, repetitive behavior, and altered anxiety (Irwin et al., 2001; Hutsler and Zhang, 2010; Dansie et al., 2013; Wu et al., 2017). We performed the marble-burying test, which indicates repetitive behavior, and the three-chamber social interaction test (Crawley, 2007; Moy et al., 2008; Silverman et al., 2010) on *Prmt8* homozygous mice and wild-type littermates (~P45). Mice of the two genotypes displayed similar scores in the marble-burying test and preference to interact with unfamiliar mice as opposed to the inanimate cage

Figure 2. PRMT8 Regulates Dendritic Spine Maturation

(A) Knockdown of PRMT8 by shRNAs in cultured cortical neurons. Results were pooled from two independent experiments.

(B) Hippocampal neurons were cotransfected with GFP and the PRMT8-shRNA or control shRNA with or without the RNAi-resistant PRMT8 construct. The density of the individual spine type was quantified. Results were pooled from two independent experiments; 40 dendrites in each group were quantified. Data were mean ± SEM; *$p < 0.05$, ****$p < 0.0001$; one-way ANOVA, Tukey's multiple comparison test (density of mushroom spine, total protrusion, and percentage of spine types); Kruskal-Wallis test, Dunn's multiple comparison test (density of stubby spine, thin spine, and filopodia). Scale bars: 20 μm (upper) and 5 μm (lower).

(C) Only the RNAi-resistant wild type (WT), not the nuclear-restricted mutant (G2A-NLS), of PRMT8 could rescue the spine defects induced by the PRMT8-shRNA. Results were pooled from two independent experiments; 46–66 dendrites in each group were quantified. Data were mean ± SEM; ****$p < 0.0001$; Kruskal-Wallis test, Dunn's multiple comparison test. Scale bar: 5 μm.

(D) Hippocampal neurons were cotransfected with GFP and the control shRNA or PRMT8-shRNA with or without the RNAi-resistant WT, G121A mutant, or K107R mutant of PRMT8. Scale bar: 5 μm. Results were pooled from three independent experiments; 46–73 dendrites in each group were quantified. Data were mean ± SEM; ****$p < 0.0001$; Kruskal-Wallis test, Dunn's multiple comparison test.

(E) tdTomato and control shRNA or PRMT8-shRNA were injected and electroporated into mouse embryo at embryonic day (E) 15. Representative images showing the secondary apical dendrites from hippocampal CA1 neurons of the injected mice at P21 after staining by RFP antibody. Scale bar: 5 μm. Mushroom spines are indicated by white arrows. The density of filopodia (yellow arrows) was significantly increased in mice introduced with the PRMT8-shRNA compared with control. Results were pooled from two independent experiments; 12–19 dendrites from 4 mice in each experimental group were quantified. Data were mean ± SEM; *$p < 0.05$; Student's t test (density of mushroom spines), Mann-Whitney test (density of filopodia).

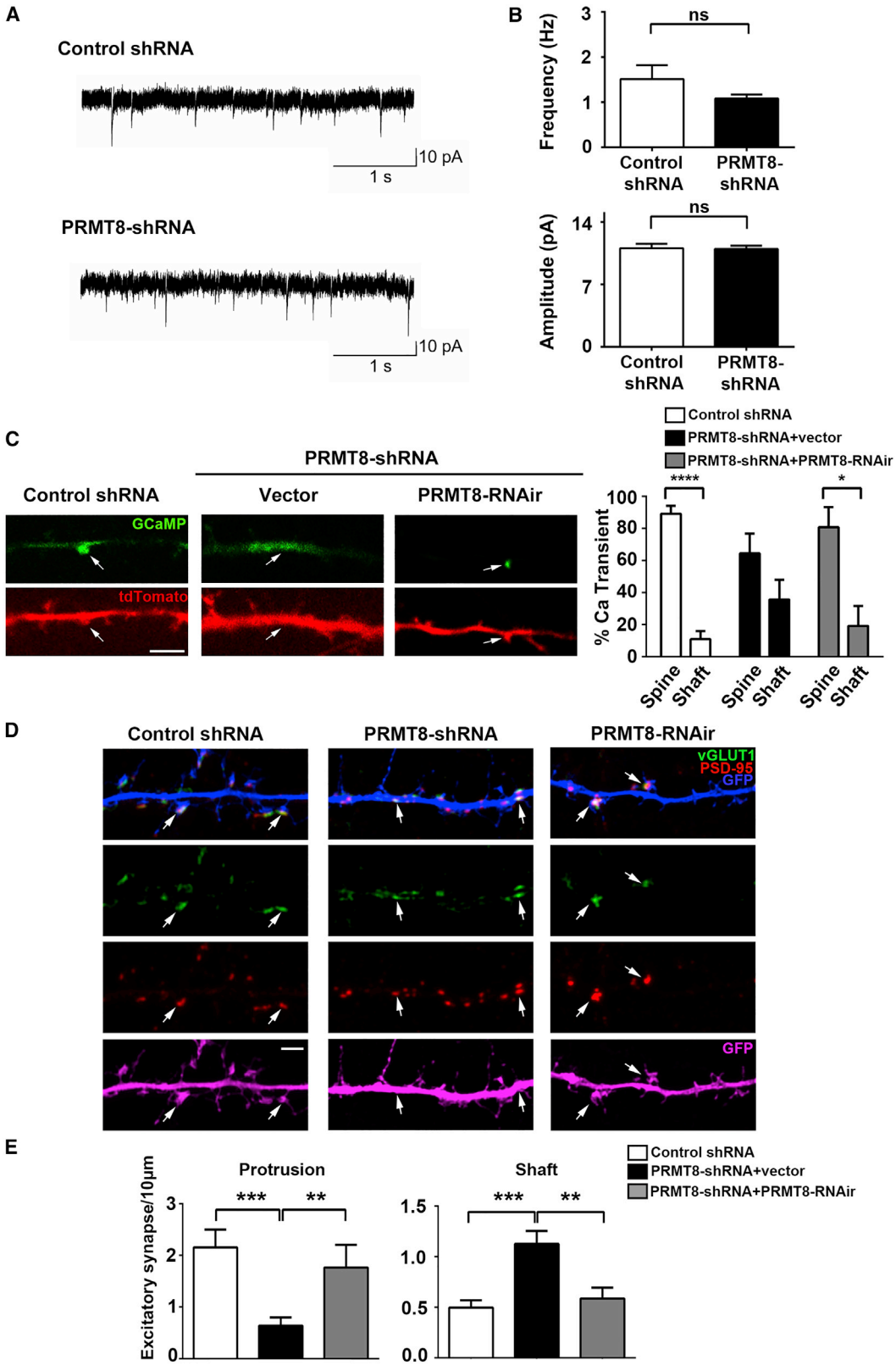

(legend on next page)

(Figures S3A and S3D). Moreover, neither social memory in the three-chamber assay nor reciprocal social interaction of freely moving mice (McFarlane et al., 2008; Chadman et al., 2008) was affected in the absence of PRMT8 (Figures S3B and S3D). Olfaction was also normal in the *Prmt8* knockout mice (Figure S3C). However, in an open-field test, the *Prmt8*-deficient mice spent significantly more time in the central zone of the arena, whereas the total travel distance was not affected (Figure 4E), suggesting reduced anxiety in the homozygous knockout mice. The anxiolytic behavior was verified by the elevated plus maze test, in which the *Prmt8* knockout mice exhibit a significant increase in the number of entries, travel distance, and time spent in the open arms (Figure 4F). Therefore, findings on the *Prmt8* knockout mice support an important physiological role of PRMT8 in spine morphogenesis, and absence of PRMT8 alters selective animal behaviors.

PRMT8 Regulates Actin Dynamics in the Dendritic Spine through Rac1-PAK1 Signaling

How does PRMT8 regulate dendritic spine maturation? The control of spine length and the conversion between mushroom spines and filopodia depend on re-organization of actin filaments (Hotulainen et al., 2009; Cheadle and Biederer, 2012). We found that some PRMT8-GFP puncta in dendrites partially overlapped with the phalloidin-positive F-actin-rich hotspots (19.8% ± 2.43% of phalloidin-labeled puncta showed overlap with PRMT8 puncta, and 15.7% ± 1.93% of PRMT8 puncta showed overlap with phalloidin-labeled puncta; mean ± SEM; 1,069 phalloidin puncta and 1,254 PRMT8 puncta from 11 dendrites were analyzed; Pearson's coefficient 0.585 ± 0.042) (Figure 5A). Time-lapse imaging of neurons expressing PRMT8-GFP and mCherry-LifeAct, which encoded a peptide that binds preferentially to F-actin, revealed that the amount of PRMT8-GFP was reduced in those dendritic spines that showed an increased LifeAct signal over time and hence were undergoing actin polymerization (Figure 5B). Furthermore, the ratio of F-actin to globular actin (G-actin) was increased in *Prmt8* homozygous knockout neurons (Figure 5C). These findings suggest that PRMT8 might negatively regulate actin polymerization locally at dendritic spines, and the increased number of filopodia in *Prmt8* knockout neurons might be attributed to altered actin cytoskeleton. To examine actin dynamics, we performed fluorescence recovery after photobleaching (FRAP) in neurons expressing mCherry-LifeAct. FRAP of LifeAct in the dendritic spine is largely reduced by the F-actin stabilization drug jasplakinolide (Rocca et al., 2013), indicating its utility to monitor actin turnover in neurons as previously shown (Njoo et al., 2015; Gokhale et al., 2016; Tong et al., 2018; Anbalagan et al., 2019). Depletion of PRMT8 by either shRNA or gene knockout significantly reduced LifeAct recovery in dendritic spines, as indicated by the decrease in dynamic fraction (Figure 5D; Figure S4), which suggests slower F-actin turnover (George et al., 2015; Anbalagan et al., 2019).

One major target for which multiple signaling pathways converge to regulate actin dynamics is the actin depolymerization factor cofilin. Upon phosphorylation at Ser-3 by LIM kinase, the actin-severing activity of cofilin is inhibited, leading to F-actin stabilization that may underlie the overabundance of elongated spines and filopodia (Hotulainen et al., 2009; Kashima et al., 2016; Pyronneau et al., 2017). We found that phosphorylation of cofilin at Ser-3 was upregulated in *Prmt8* knockout brain (Figure 5E). The increased cofilin phosphorylation was accompanied by elevated activity of the small GTPase Rac1 and phosphorylation of its downstream kinase PAK1, which is the upstream regulator of LIM kinase (Figures 5F and 5G).

One of the upstream activators of Rac1 is CYFIP1, which is also a suppressor of protein translation by preventing eIF4E binding to eIF4G (Napoli et al., 2008; De Rubeis et al., 2013). Increase in eIF4E-eIF4G interaction during translation initiation relocates CYFIP1 to the WRC-Rac1-GTP complex and activates PAK1 signaling and cofilin phosphorylation, thereby coordinating protein synthesis with actin dynamics (Santini et al., 2017). We therefore ask whether the elevated PAK1 and cofilin phosphorylation in *Prmt8* knockout brain is associated with changes in translation initiation factors. Indeed, the amount of eIF4G that binds to capped mRNA was significantly increased in the absence of PRMT8, whereas the expression of eIF4G and eIF4E was unchanged (Figure 5H; Figure S5). To ask whether the elevated PAK1 kinase activity is responsible for the spine maturation defects, neurons transfected with control shRNA or PRMT8-shRNA were treated with the PAK1 inhibitor FRAX486. Although pharmacological inhibition of PAK1 did not affect spine morphogenesis, the inhibitor abolished the immature spine phenotypes induced by PRMT8-shRNA (Figure 5I). Our findings indicate that PRMT8 promotes dendritic spine maturation by keeping the Rac1-PAK1 pathway under control through translation initiation factors. Depletion of PRMT8 impairs F-actin severing by overinhibition of cofilin, which stabilizes the otherwise-transient filopodia.

Figure 3. PRMT8 Regulates the Localization of Excitatory Synapses between the Dendritic Spines and the Dendritic Shaft

(A) Patch-clamp recording of the mEPSC was performed on hippocampal neurons transfected with control shRNA or PRMT8-shRNA. (B) Quantification revealed no significant difference in either the frequency or the amplitude of mEPSC between control and PRMT8 knockdown neurons. 6 neurons in each experimental group were quantified. $p > 0.05$; Student's t test.

(C) Hippocampal neurons were cotransfected with tdTomato and the calcium indicator GCaMP6, together with control shRNA or PRMT8-shRNA with or without the RNAi-resistant PRMT8 construct. Live imaging of Ca^{2+} transient events were taken by spinning disk confocal microscopy (0.3 ms per interval). Scale bar: 5 μm. Results were pooled from two independent experiments; 8–11 dendrites in each experimental group were quantified. Data were mean ± SEM; $^{*}p < 0.05$, $^{****}p < 0.0001$; Student's t test (comparison between shaft and protrusion synapses for the experimental group of PRMT8-shRNA), Mann-Whitney test (comparison between shaft and protrusion synapses for the experimental groups of control shRNA and PRMT8-shRNA + RNAi-resistant PRMT8).

(D) Confocal images of hippocampal neuronal dendrites (15 DIV) expressing GFP (blue) and the indicated DNA constructs and costained by vGLUT1 (green) and PSD-95 (red). Arrows indicate vGLUT1/PSD-95 puncta. Scale bar: 2 μm.

(E) Depletion of PRMT8 resulted in mislocalization of excitatory synapses from dendritic spines to the dendritic shaft. Results were pooled from two independent experiments; 14–20 dendrites in each group were quantified. Data were mean ± SEM; $^{**}p < 0.01$, $^{***}p < 0.001$; one-way ANOVA, Tukey's multiple comparison test (shaft synapses); Kruskal-Wallis test, Dunn's multiple comparison test (synapses on protrusions).

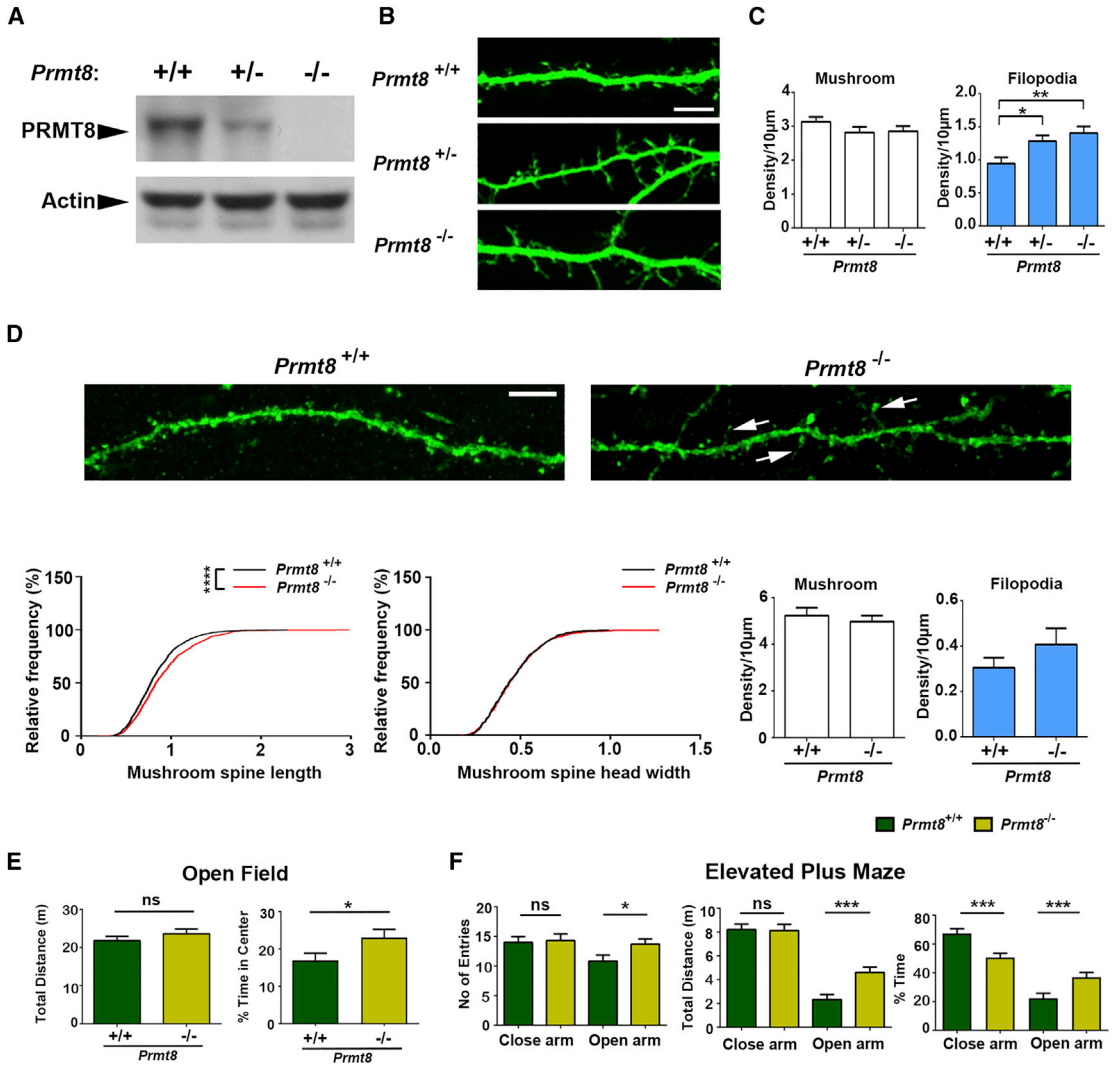

Figure 4. Spine Maturation Defects and Animal Behavior of *Prmt8* Knockout Mice

(A) Expression of PRMT8 in WT (+/+), heterozygous (+/−), and homozygous (−/−) knockout mouse brains.

(B) Dissociated hippocampal neurons were isolated from WT, heterozygous, and homozygous *Prmt8* knockout mice. Neurons were transfected with GFP at 13 DIV and stained at 16 DIV with GFP antibody. Scale bar: 5 μm.

(C) Density of filopodia in *Prmt8* homozygous and heterozygous neurons was significantly greater than in WT neurons. Results were pooled from four independent experiments; 27–41 dendrites of each genotype were quantified. Data were mean ± SEM; *p < 0.05, **p < 0.01; Kruskal-Wallis test, Dunn's multiple comparison test.

(D) AAV5 carrying YFP-expressing construct was stereotaxically injected into hippocampi of WT and *Prmt8* homozygous knockout mice. Representative images of the GFP-positive secondary apical dendrites from hippocampal CA1 neurons of the injected mice (6 weeks old) were shown. Elongated spines (arrows) were observed in dendrites of the *Prmt8* homozygous knockout mice. Scale bar: 5 μm. Cumulative frequency curve showing significant increase in the length, but not the head width, of mushroom spines in *Prmt8* homozygous knockout neurons compared with WT control. No significant difference in mushroom spine or filopodia density was observed between genotypes. Results were pooled from two independent experiments; 28–31 dendrites for each genotype were quantified. Data were mean ± SEM; ****p < 0.0001; Mann-Whitney test.

(E) No significant difference in total travel distance between WT and *Prmt8* homozygous knockout mice was observed in the open-field test, but the *Prmt8* homozygous knockout mice spent significantly more time in the center compared with WT littermates. 22 mice (11 male and 11 female) of each genotype were analyzed. Data were mean ± SEM; *p < 0.05; Student's t test.

(F) The number of entries, total travel distance, and time spent in the open arms in the elevated plus maze were significantly increased in *Prmt8* homozygous knockout mice compared with WT littermates. 23 mice (12 male and 11 female) of each genotype were analyzed. Data were mean ± SEM; *p < 0.05, ***p < 0.001; Student's t test.

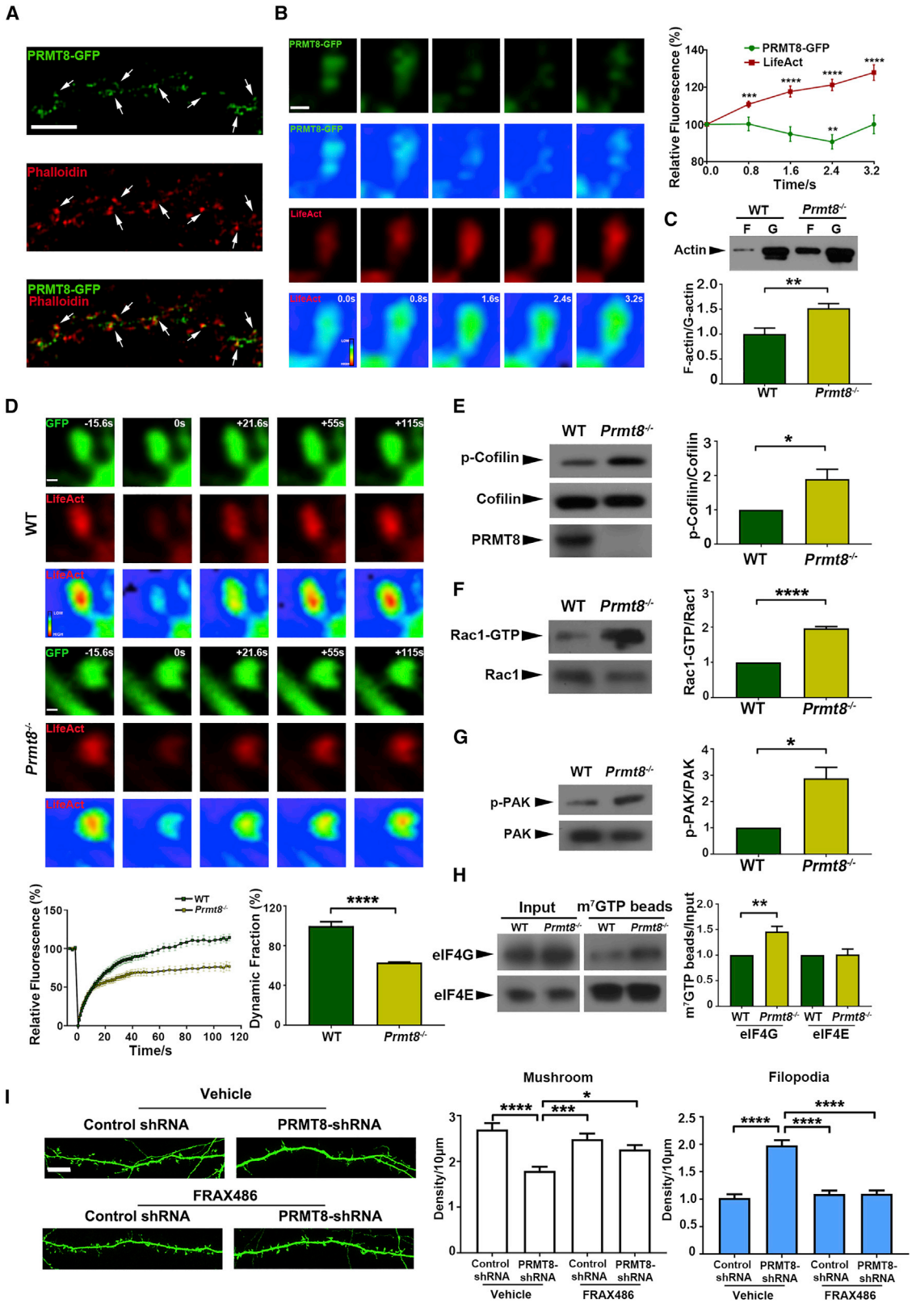

(legend on next page)

G3BP1 Acts Downstream of PRMT8 in Dendritic Spine Maturation and the Control of Actin Dynamics

To gain insight into how PRMT8 regulates F-actin dynamics and spine maturation in neurons, we performed pull-down experiments followed by mass spectrometry to identify potential PRMT8 methylation substrates. By comparing the putative PRMT8-interacting proteins with large-scale proteomic studies of arginine-methylated proteins (Ong et al., 2004; Guo et al., 2014), we focused on two RBPs: RasGAP SH3 domain binding proteins 1 and 2 (G3BP1 and G3BP2). G3BP1 and G3BP2 are essential for the formation of stress granules, but their functions in neurons under unstressed condition are poorly defined. G3BP1 and G3BP2 were expressed in neuronal dendrites and SNS (Figure S6), and both interacted with PRMT8 (Figure 6A). The interaction was specific, because Staufen1 and Septin-7, which are implicated in spine maturation (Tada et al., 2007; Xie et al., 2007; Vessey et al., 2008) and arginine methylated in the brain (Guo et al., 2014), did not bind to PRMT8. Either G3BP1-shRNA or G3BP2-shRNA reduced mushroom spine density in hippocampal neurons, but only knockdown of G3BP1, not G3BP2, specifically increased the number of filopodia (Figures 6B and 6C; Figure S7). Therefore, depletion of G3BP1 mimics the immature spine phenotypes in PRMT8-depleted neurons. Immunocytochemistry revealed that G3BP1 was largely excluded from the nucleus (Figure 6D) but was detected in dendrites (Figure S7C), in which it was present in subsets of dendritic spines (Figure S6A), and their localization partially overlapped with PRMT8 (Figure 6E) (10.0% ± 1.1% PRMT8 puncta overlapped with G3BP1 puncta, and 9.37% ± 0.94% G3BP1 puncta overlapped with PRMT8 puncta; mean ± SEM; 1,254 PRMT8 puncta and 1,345 G3BP1 puncta from 11 dendrites were analyzed; Pearson's coefficient 0.386 ± 0.069). The low degree of overlap between PRMT8 and G3BP1 might be explained by the rapid dissociation of substrate following methylation (Feng et al., 2011), and presumably G3BP1 is released from the membrane-bound PRMT8 to exert its function in the cytoplasm.

PRMT8 induces asymmetric dimethylation of G3BP1 *in vitro* (Tsai et al., 2016), but the role of this methylation in neurons remains unknown. We found that G3BP1 was dimethylated in the SNS, and importantly, the methylation was significantly reduced by *Prmt8* knockout, suggesting that PRMT8 is one of the major methyltransferases of G3BP1 in neurons (Figure 6F). To investigate the biological significance of G3BP1 arginine methylation, we first mapped the major methylated arginine residues. Two arginine residues, R433 and R445, in the RGG domain of G3BP1 can undergo methylation (Bikkavilli and Malbon, 2011; Guo et al., 2014). The arginine methylation on G3BP1 was abolished when both R433 and R445 were substituted to histidine, thereby confirming the two arginine residues as major methylated sites (Figure 6G).

In stress granules, G3BP1 interacts with the translation initiation complex (Panas et al., 2016; Yang et al., 2019). We found that G3BP1 interacted with eIF4E, but not eIF4G, and binding was abolished in the methylation-deficient G3BP1 (Figure 6H). To address the importance of G3BP1 methylation in spine maturation, we compared the effect of wild type and the methylation-deficient G3BP1 mutant (R433/445H) on dendritic spine morphology. Coexpression of wild type, but not the methylation-deficient G3BP1, could reverse the overproduction of filopodia upon knockdown of G3BP1 (Figure 7A). Similar to the PRMT8-depleted neuron, G3BP1-shRNA reduced LifeAct FRAP in dendritic spines, and the change in F-actin dynamics was rescued only by the wild type, not methylation-deficient G3BP1 (Figure 7B). Therefore, G3BP1 promotes spine maturation through the control of actin

Figure 5. PRMT8 Regulates Actin Cytoskeleton and Spine Maturation through the Rac1-PAK1-Cofilin Signaling Pathway

(A) Subcellular localization of PRMT8-GFP (green) and F-actin (red, indicated by phalloidin staining) in dendrites. Hippocampal neurons were transfected with the PRMT8-GFP expression construct at 13 DIV, followed by immunofluorescence staining at 20 DIV. PRMT8 puncta in F-actin-enriched regions are indicated (arrows). Scale bar: 5 μm.

(B) Spinning disk confocal imaging of hippocampal neurons coexpressing PRMT8-GFP and mCherry-LifeAct. Representative images showing the dynamic of PRMT8-GFP (green) at dendritic spines undergoing actin polymerization, as indicated by the increase in the LifeAct signal (red) over time. Neurons were transfected at 14 DIV and imaged at 18 DIV. PRMT8-GFP signal intensity decreased in dendritic spines that showed increased LifeAct signals at different time points. 22 spines from 8 cells were quantified. Data were mean ± SEM; $^{**}p < 0.01$, $^{***}p < 0.001$, $^{****}p < 0.0001$ compared with the fluorescence intensity at 0 s; Kruskal-Wallis test, Dunn's multiple comparison test. Scale bar: 1 μm.

(C) Increased ratio of F-actin to G-actin in cultured cortical neurons from *Prmt8* homozygous knockout (*Prmt8*$^{-/-}$) mice compared with WT neurons. Neurons from 7–8 mice of each genotype were quantified. Data were mean ± SEM; $^{**}p < 0.01$, Student's t test.

(D) Fluorescence recovery of mCherry-LifeAct in dendritic spines of hippocampal neurons from WT or *Prmt8*$^{-/-}$ mice cotransfected with GFP and mCherry-LifeAct. FRAP curves were plotted based on the recovered mCherry-LifeAct fluorescence normalized to pre-bleach intensity. Histograms showed the percentage of F-actin dynamic fractions in dendritic spines was significantly reduced in *Prmt8* knockout neurons. Results were pooled from three independent experiments; 23–31 spines from 10–11 neurons were quantified for each condition. Data were mean ± SEM; $^{****}p < 0.0001$; Student's t test. Scale bar: 1 μm.

(E) Increased phosphorylated cofilin (p-cofilin)-to-cofilin ratio was observed in *Prmt8*$^{-/-}$ brain compared with WT brain. 5–6 mice of each genotype were quantified. Data were mean ± SEM; $^{*}p < 0.05$; Student's t test.

(F) Western blot showing the activated Rac1 (Rac1-GTP) and total Rac1 in the brain lysate of WT or *Prmt8*$^{-/-}$ mice. An increased Rac1-GTP-to-total Rac1 ratio was observed in *Prmt8*$^{-/-}$ mice compared with WT mice. 3 mice of each genotype were quantified. Data were mean ± SEM; $^{****}p < 0.0001$; Student's t test.

(G) Increased PAK1 phosphorylation in *Prmt8*$^{-/-}$ brain. Western blot showing the phosphorylated PAK1 (p-PAK) and total PAK1 in the brain lysates of WT or *Prmt8*$^{-/-}$ mice. 3 mice of each genotype were quantified. Data were mean ± SEM; $^{*}p < 0.05$; Student's t test.

(H) Increased eIF4G in the translation initiation complex of *Prmt8*$^{-/-}$ brain. eIF4G was pulled down with m^{7}GTP beads from the brain lysate. 3 mice of each genotype were quantified. Data were mean ± SEM; $^{**}p < 0.01$; Student's t test.

(I) Hippocampal neurons (13 DIV) were cotransfected with GFP and control shRNA or PRMT8-shRNA, followed by GFP staining. Inhibition of PAK by FRAX486 (500 nM for 2 h) abolished the reduction of mushroom spine density and increase in filopodia density induced by PRMT8 knockdown. Results were pooled from three independent experiments; 60–85 dendrites were quantified for each condition. Data were mean ± SEM; $^{*}p < 0.05$, $^{***}p < 0.001$, $^{****}p < 0.0001$; Kruskal-Wallis test, Dunn's multiple comparison test. Scale bar, 10 μm.

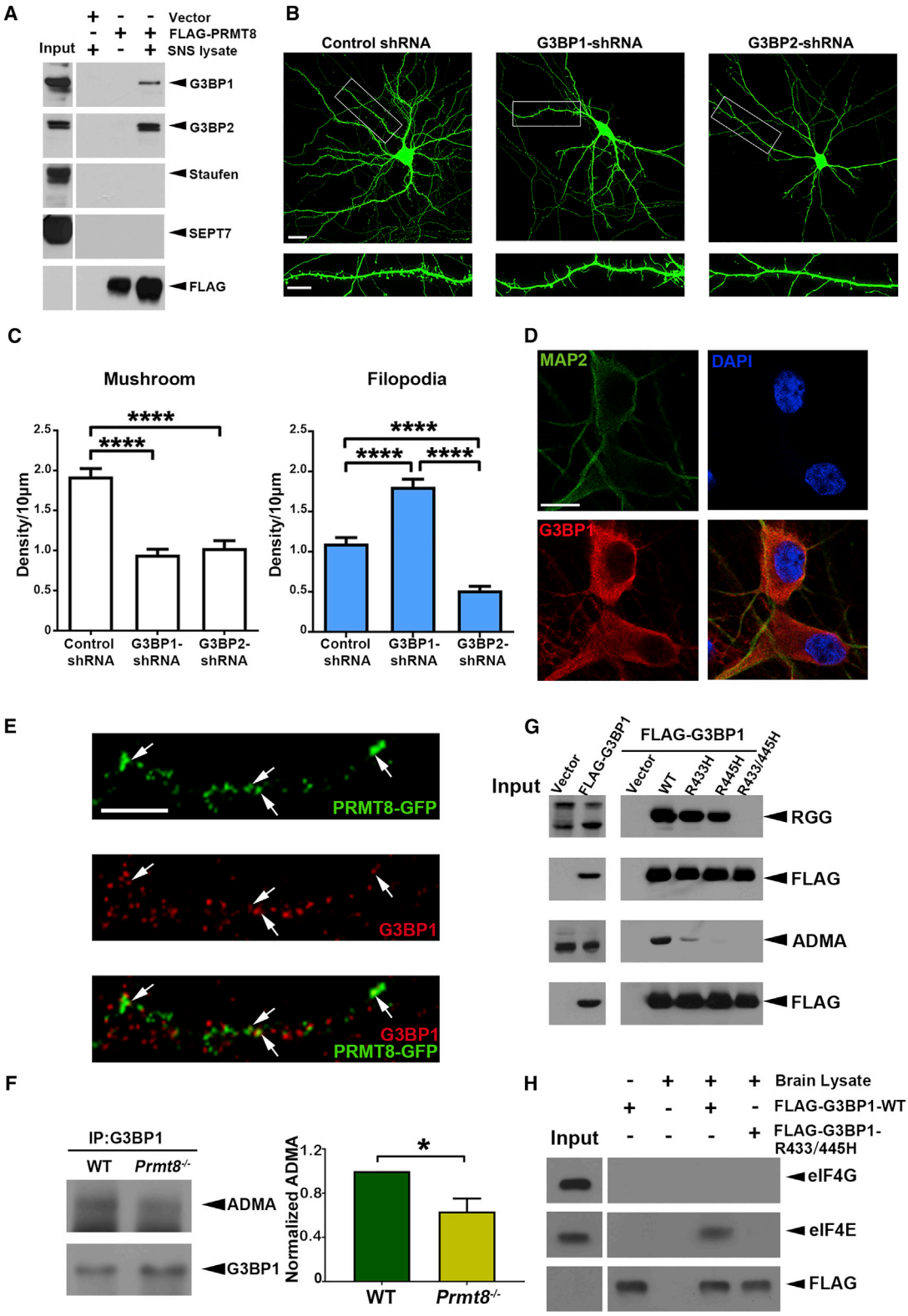

(legend on next page)

dynamics, and its action depends on arginine methylation within the RGG domain.

If G3BP1 is a major downstream target of PRMT8, we reason that the immature spine phenotypes observed in G3BP1-depleted neurons should be reversed by PAK1 inhibition. Treatment with the PAK inhibitor FRAX486 abolished the increase in filopodia density after G3BP1 knockdown (Figure 7C). Altogether, our findings reveal a crucial role for both PRMT8 and its downstream target G3BP1 in suppressing the overproduction of filopodia during dendritic spine maturation, and this process involves regulation of actin cytoskeleton by cofilin through tight control of Rac1 and PAK1 activity.

DISCUSSION

Arginine methylation was discovered as a protein post-translational modification (PTM) decades ago (reviewed by Paik et al., 2007), but its importance in the brain has only begun to be explored recently. Here we present compelling evidence to support PRMT8, a brain-restricted PRMT, as a key player in the control of dendritic spine maturation in neurons. Consistent with a previous study (Penney et al., 2017), we found that PRMT8 is not enriched in the nucleus and it is present in dendrite and dendritic spine. Expression of a nuclear-restricted PRMT8 cannot rescue the spine defects in PRMT8-deficient neurons. We further provide evidence that G3BP1, a dendritically localized RBP that is absent in the nucleus, is one of the PRMT8 substrates and downstream targets that promotes spine maturation through PAK1 signaling and modulation of actin cytoskeleton. The importance of protein arginine methylation in gene transcription and RNA metabolism within the nucleus has been well documented. However, despite the identification of many methylated cytoplasmic proteins by proteomic studies, the role of arginine methylation in neuronal cytoplasm is far from clear. Our findings have unraveled a non-nuclear role of PRMT8 in promoting synapse maturation through local regulation of actin cytoskeleton, thereby providing new insights into the multi-faceted function of arginine methylation.

In a previous study, the densities of different spine types in hippocampal CA1 neuron were similar between wild-type and *Prmt8* null mice (Penney et al., 2017). In our study, the densities of mushroom spines and filopodia in hippocampal neurons *in vivo* are also similar between wild-type and *Prmt8* knockout mice, but the length of the dendritic spines is significantly increased in mice lacking PRMT8. The mice that were examined by Penney et al. (2017) were considerably older (10–14 weeks) than those in our study (6 weeks). There might be differential effects of PRMT8 on spine morphology at different ages. In support of this, overabundance of filopodia *in vivo* was only observed in P21 mice upon PRMT8 knockdown by *in utero* electroporation, not in 6-week-old *Prmt8* knockout mice. It is possible that as the brain becomes more mature, compensatory pathways help to correct the delayed spine maturation.

Increased filopodia and elongated dendritic spines in fragile X syndrome are associated with autism (Dictenberg et al., 2008). We did not observe abnormal sociability or social memory in the three-chamber assay for the *Prmt8* knockout mice. The social behavior of freely moving mice and marble burying, an indication of repetitive behavior, were also indistinguishable between *Prmt8* null mice and their wild-type littermates. Interestingly, the *Prmt8*-deficient mice exhibit anxiolytic behaviors in the open-field test and the elevated plus maze. In this regard, mice deficient in neurabin and spinophilin, two closely related actin-binding proteins that are involved in dendritic spine maturation (Feng et al., 2000), and *Fmr1* null mice display anxiolytic behavior (Kim et al., 2011; Dansie et al., 2013; Wu et al., 2017). Therefore, besides learning and memory, other brain functions such as affective behavior might depend on proper actin dynamics and spine morphogenesis.

F-actin is abundant in dendritic spines, and uncontrolled actin dynamics can induce spine elongation and production of filopodia (Hotulainen et al., 2009; Pyronneau et al., 2017). We provide multiple lines of evidence to demonstrate the link between PRMT8 and actin dynamics. First, PRMT8 localization is decreased over time in dendritic spines that undergo elevated F-actin polymerization. Second, FRAP experiments revealed that depletion of PRMT8 through either shRNA or gene knockout reduces actin dynamics or turnover within dendritic spines, which may indicate increased F-actin stabilization (Hotulainen et al., 2009; Rocca et al., 2013; Tong et al., 2018; Anbalagan et al., 2019) or reduced actin polymerization (Njoo et al., 2015; Gokhale et al., 2016). Although the FRAP data alone do not

Figure 6. Arginine Methylation of the PRMT8 Binding Protein G3BP1 and the Role of G3BP1 in Dendritic Spine Maturation

(A) Specific pull-down of G3BP1 and G3BP2, but not the two other methylated proteins, Staufen and Septin7, from SNS by PRMT8. HEK293T cells were transfected with the FLAG-PRMT8 expression construct or vector. FLAG beads were used to immunoprecipitate FLAG-PRMT8 from the HEK293T cell lysate, followed by pull-down assay upon incubation with mouse SNS.

(B) Effect of G3BP1 or G3BP2 knockdown on mushroom spines and filopodia. Representative images were shown. Scale bars: 20 μm (upper) and 10 μm (lower).

(C) Differential effects of G3BP1-shRNA and G3BP2-shRNA on the density of filopodia. Results were pooled from two independent experiments; 39–66 dendrites were quantified for each condition. Data were mean ± SEM; ****$p < 0.0001$, Kruskal-Wallis test, Dunn's multiple comparison test.

(D) Images of primary hippocampal neurons (10 DIV) stained with MAP2 (green), DAPI (blue), and G3BP1 (red). Little G3BP1 immunoreactivity was detected in the nucleus. Scale bar: 10 μm.

(E) Subcellular localization of GFP-tagged PRMT8 (green) and G3BP1 (red) in dendrites. Primary hippocampal neurons were transfected with PRMT8-GFP at 13 DIV, followed by immunostaining at 20 DIV. Examples of overlapped PRMT8 and G3BP1 puncta are indicated (arrows). Scale bar: 5 μm.

(F) Reduced asymmetric dimethylation of G3BP1 in the SNS of *Prmt8*$^{-/-}$ mice revealed by western blot using asymmetric dimethyl arginine (ADMA) antibody. 4 mice of each genotype were quantified. Data were mean ± SEM; $p < 0.05$; Student's t test.

(G) Various FLAG-tagged G3BP1 constructs were transfected into HEK293T cells and immunoprecipitated by FLAG beads. Substituting the two arginine residues (Arg-433 and Arg-445) with histidine abolished mono-methylation (RGG) and asymmetric dimethylation (ADMA).

(H) eIF4E was pulled down from mouse brain by FLAG-tagged WT, but not the methylation-deficient G3BP1. HEK293T cells were transfected with the indicated constructs. Following immunoprecipitation by FLAG beads, the proteins were incubated with mouse brain lysate, followed by western blot with the indicated antibodies.

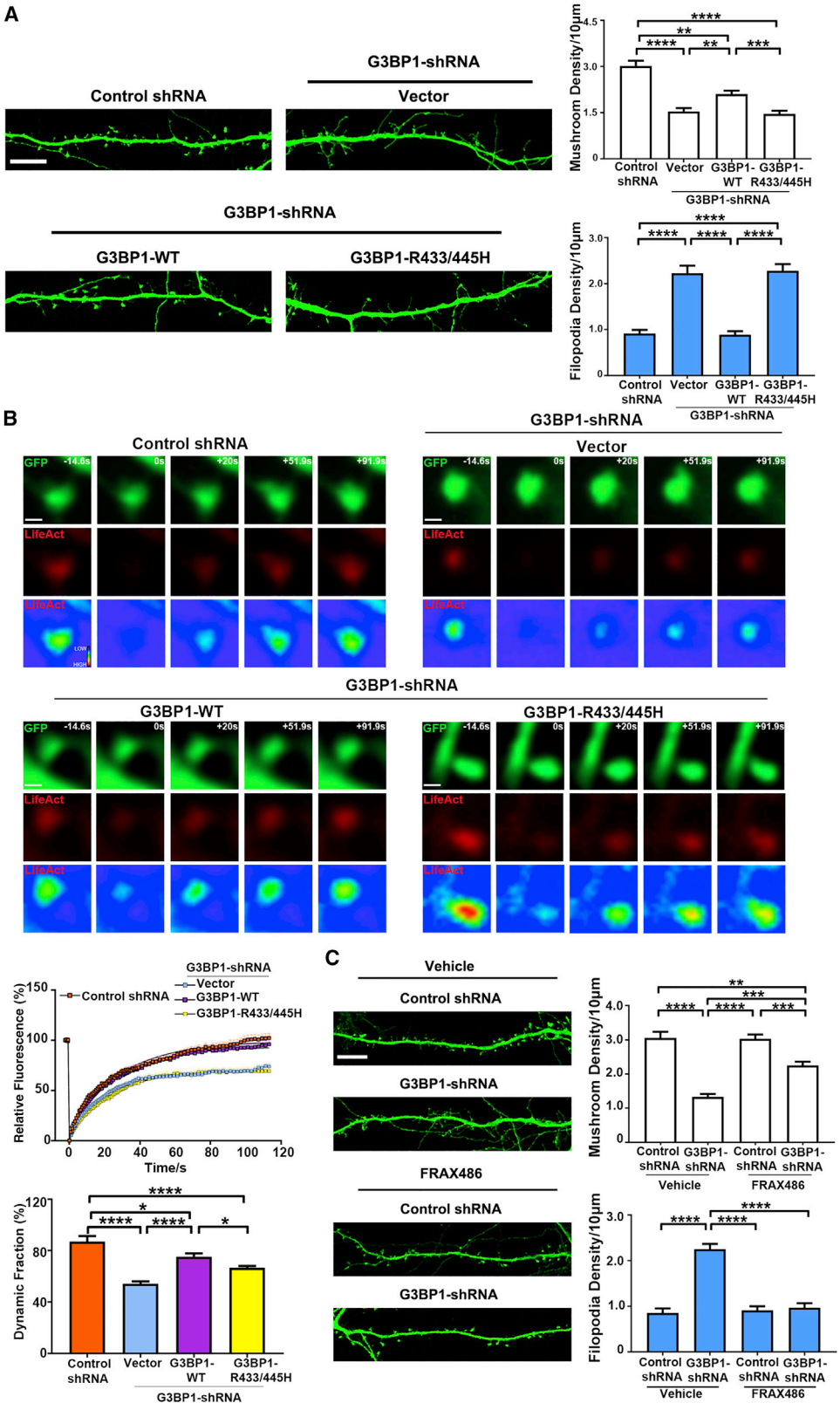

(legend on next page)

distinguish between these two possibilities, the increased F-actin-to-G-actin ratio in PRMT8-depleted neurons favors the interpretation of increased F-actin stability. Consistent with this notion, the activity of Rac1, which inhibits the actin-depolymerizing factor cofilin through PAK1 and LIM kinase, as well as Ser-3 phosphorylation of cofilin, are both enhanced in *Prmt8* knockout brain. Finally, PAK1 inhibition by FRAX486 reverses the immature filopodia induced by PRMT8 knockdown. Our findings indicate that PRMT8 maintains proper dendritic spine morphology by keeping the Rac1-PAK1 signaling and cofilin activity under control. Loss of PRMT8 subsequently leads to uncontrolled actin dynamics and stabilizes the elongated filopodia. Another PRMT, PRMT2, controls actin cytoskeleton during dendritic growth by inducing methylation of the actin-nucleation factor Cobl (Hou et al., 2018). Therefore, arginine methylation represents an emerging major PTM that intricately controls neuronal actin cytoskeleton via multiple actin-binding proteins. Nonetheless, although we have delineated the control of actin cytoskeleton by cofilin as the underlying mechanism of PRMT8 in spine maturation, we do not rule out the possibility that PRMT8 exerts its synaptic effect through other cellular processes, including gene transcription. Indeed, PRMT8 regulates dendritic arborization through transcriptional control of Tenascin-R, a component of the peri-neuronal net (Lee et al., 2017). Moreover, less than half of the dendritic PRMT8 puncta overlap with PSD-95 or present in dendritic spines, suggesting that PRMT8 has dendritic functions outside the synapses. Future proteomic studies that identify differentially methylated proteins between control and *Prmt8* knockout brains are crucial to decipher the multiple substrates and diverse functions of PRMT8.

How does PRMT8 regulate Rac1-PAK1 signaling and actin to control spine maturation? PRMT8 is unusual among the various PRMTs, because it possesses the dual activities of phospholipase D and arginine methyltransferase (Kim et al., 2015). Although PRMT8 might exert its effect through phospholipase D activity, which regulates actin cytoskeleton through Rac1 (Rudge and Wakelam, 2009), in our rescue experiments, the phospholipase D-deficient mutant is capable of reversing the spine maturation defects in PRMT8 knockdown neurons, suggesting that the effect of PRMT8 is mediated via arginine methylation. Toward this end, we identify G3BP1 as a downstream target of PRMT8 that plays a crucial role in dendritic spine maturation. G3BP1 is essential for the formation of stress granules in response to diverse cellular stress stimuli, but there is little information about its physiological function in neurons under normal conditions. G3BP1-deficient mice exhibit impaired synaptic plasticity (Martin et al., 2013), suggesting its possible role in regulating synaptic function. We demonstrate here that G3BP1 is expressed in dendrites and dendritic spines. Similar to PRMT8-deficient neurons, G3BP1 depletion leads to increased filopodia density that is fully rescued by inhibition of PAK1. In parallel experiments, knockdown of the related protein G3BP2 leads to reduction instead of increase in filopodia. Therefore, the two homologous RBPs play different roles in spine morphogenesis, which agrees with their distinct functions in non-neuronal cells, in which they differentially affect cell proliferation and may bind to different proteins and mRNAs (Winslow et al., 2013; Alam and Kennedy, 2019). Although the precise mechanism by which PRMT8 and G3BP1 regulate Rac1-PAK1 signaling remains to be determined, one possibility involves the translation initiation complex. In the m^7GTP bead pull-down assay, there is increased abundance of eIF4G in the translation initiation complex of *Prmt8* knockout brain. Moreover, G3BP1 interacts with eIF4E, which depends on the two arginine methylation sites on G3BP1. Given that G3BP1 assembles stress granules that contain the translation initiation complex (Panas et al., 2016), and G3BP1 is able to repress translation in stress-granule-like small aggregates without stress stimulus (Ortega et al., 2010; Sahoo et al., 2018), it is conceivable that PRMT8 depletion and reduced methylation of G3BP1 will decrease the binding of G3BP1 to eIF4E and release the translation repression. The resulting enhanced translation might shift more CYFIP1 to the Rac1-WAVE1 complex, leading to overactivation of this pathway that causes PAK1 hyperphosphorylation and overinhibition of cofilin. Dysregulation of the Rac1-PAK1 signaling because of altered eIF4E-eIF4G interaction contributes to spine defects in *Fmr1* null mice (Pyronneau et al., 2017; Santini et al., 2017). In this context, it is noteworthy that G3BP1 shares a binding partner, Caprin1, with FMRP, and the two RBPs can coexist in RNA granules (Solomon et al., 2007; El Fatimy et al., 2012; Shiina, 2019). Furthermore, both *Fmr1* null mice and *G3bp1* knockout mice show enhanced hippocampal long-term depression (Huber et al., 2002; Hou et al., 2006; Martin et al., 2013). It will be interesting to elucidate the potential cross-talk between G3BP1 and FMRP in the future.

RBPs represent a major class of substrates for PRMTs (Bedford and Richard, 2005), and RNA processing within the nucleus, such as splicing, stability, and nuclear export, critically depends on arginine methylation of various RBPs (Blackwell and Ceman, 2012). Although the current study focuses on G3BP1, other dendritically localized RBPs, such as FMRP, Staufen, and Sam68, can also undergo arginine methylation (Côté et al., 2003;

Figure 7. G3BP1 Regulates F-actin Turnover and Spine Maturation through PAK1 and the Importance of G3BP1 Arginine Methylation

(A) Regulation of dendritic spine maturation by G3BP1 depends on arginine methylation in the RGG domain. Hippocampal neurons were cotransfected with GFP and control shRNA or G3BP1-shRNA, together with RNAi-resistant G3BP1 constructs. Results were pooled from three independent experiments; 49–52 dendrites were quantified for each condition. Data were mean ± SEM; $^{**}p < 0.01$, $^{***}p < 0.001$, $^{****}p < 0.0001$; Kruskal-Wallis test, Dunn's multiple comparison test. Scale bar: 10 μm.

(B) Spinning disk confocal images showing the FRAP of mCherry-LifeAct in dendritic spines of hippocampal neurons. The dynamic fraction of F-actin in dendritic spines was significantly reduced after knockdown of G3BP1, which was partially rescued by coexpression of WT, but not the methylation-deficient R433/445H mutant of G3BP1. Results were pooled from three independent experiments; 29–32 spines from 9–11 neurons were quantified for each condition. Data were mean ± SEM; $^{*}p < 0.05$, $^{****}p < 0.0001$; one-way ANOVA, Tukey's multiple comparison test. Scale bars: 1 μm.

(C) Hippocampal neurons were cotransfected with GFP and the control shRNA or G3BP1-shRNA. Inhibition of PAK1 by FRAX486 (500 nM for 2 h) rescued the overproduction of filopodia induced by the G3BP1-shRNA. Results were pooled from two independent experiments; 34–43 dendrites were quantified for each condition. Data were mean ± SEM; $^{**}p < 0.01$, $^{***}p < 0.001$, $^{****}p < 0.0001$; Kruskal-Wallis test, Dunn's multiple comparison test. Scale bar: 10 μm.

Dolzhanskaya et al., 2006; Stetler et al., 2006; Blackwell et al., 2010; Klein et al., 2013; Guo et al., 2014). Arginine methylation often occurs within the RGG motif, and many RGG-motif-containing proteins are able to regulate eIF4E-eIF4G interaction (Rajyaguru and Parker, 2012). From a broader perspective, it is tempting to speculate that the arginine methylation of multiple RBPs in dendrites and the subsequent local control of the translation initiation complex could represent a key regulatory mechanism of actin dynamics, synapse development, and plasticity.

STAR★METHODS

Detailed methods are provided in the online version of this paper and include the following:

- KEY RESOURCES TABLE
- RESOURCE AVAILABILITY
  - Lead Contact
  - Materials Availability
  - Data and Code Availability
- EXPERIMENTAL MODEL AND SUBJECT DETAILS
  - Animals
  - Primary neuronal culture
- METHOD DETAILS
  - DNA constructs
  - Transfection of primary neurons
  - Preparation of synaptoneurosome (SNS)
  - Pharmacological treatment of neurons and western blot analysis
  - Immunoprecpitation and pull-down assay
  - F-actin/G-actin ratio
  - *In situ* hybridization
  - In utero electroporation, stereotaxic injection, perfusion and brain sectioning
  - Immunofluorescence staining, confocal imaging and quantitative analysis
  - Calcium imaging of hippocampal neuron
  - FRAP experiments
  - Electrophysiology
  - Animal behavioral tests
- QUANTIFICATION AND STATISTICAL ANALYSIS

SUPPLEMENTAL INFORMATION

Supplemental Information can be found online at https://doi.org/10.1016/j.celrep.2020.107744.

ACKNOWLEDGMENTS

We are grateful to Nancy Ip (Hong Kong University of Science and Technology) for the GFP expression construct, Daisy Shum (University of Hong Kong) for the pCDNA4-tdTomato construct, King-Ho Cheung (Baptist University) for the pGP-CMV-GCaMP6 construct, Karl Deisseroth (Neurosciences Institute of Stanford University) for the pAAV-CaMKIIα-eYFP construct, Florian Plattner (University of Texas Southwestern Medical Center) for advice on animal behavior experiments, and Jasmine Chit-Ying Lau for performing the olfactory habituation-dishabituation test and analysis of the three-chamber social interaction assay. We also thank Anping Chai (University of Hong Kong) for the mEPSC recording, Cora Sau-Wan Lai and Albert Hiu-Ka Fok (University of Hong Kong) for technical advice on *in utero* electroporation and animal behavioral tests, and the Imaging Core Facility from the Faculty of Medicine at the University of Hong Kong for image acquisition and analysis. This study was supported in part by the Research Grant Council of Hong Kong (General Research Fund [GRF] 16100814, 17135816, and 17106018 and Early Career Scheme [ECS] 27119715), the Area of Excellence Scheme (grant AoE/M-604/16) and the Theme-based Research Scheme (T13-605/18-W) of the University Grants Committee of Hong Kong, Health and Medical Research Fund (06172986), Hong Kong, and the Liu Po Shan/Dr. Vincent Liu Endowment Fund for Motor Neurone Disease.

AUTHOR CONTRIBUTIONS

K.-O.L. conceived and supervised the study. K.-O.L., L.H.-Y.L., and R.D. designed the experiments. L.H.-Y.L. and R.D. performed most experiments. Q.L. performed stereotaxic injection and immunohistochemistry and contributed to animal behavior experiments. L.H.-Y.L., R.D., and Q.L. analyzed the data. K.-O.L and L.H.-Y.L. wrote the original draft of the manuscript. K.-O.L., L.H.-Y.L., and R.D. revised the manuscript.

DECLARATION OF INTERESTS

The authors declare no competing interests.

Received: March 1, 2019
Revised: April 1, 2020
Accepted: May 18, 2020
Published: June 9, 2020

REFERENCES

Alam, U., and Kennedy, D. (2019). Rasputin a decade on and more promiscuous than ever? A review of G3BPs. Biochim. Biophys. Acta Mol. Cell Res. *1866*, 360–370.

Anbalagan, S., Blechman, J., Gliksberg, M., Gordon, L., Rotkopf, R., Dadosh, T., Shimoni, E., and Levkowitz, G. (2019). Robo2 regulates synaptic oxytocin content by affecting actin dynamics. eLife *8*, e45650.

Bader, P.L., Faizi, M., Kim, L.H., Owen, S.F., Tadross, M.R., Alfa, R.W., Bett, G.C., Tsien, R.W., Rasmusson, R.L., and Shamloo, M. (2011). Mouse model of Timothy syndrome recapitulates triad of autistic traits. Proc. Natl. Acad. Sci. USA *108*, 15432–15437.

Baudry, M., Kramar, E., Xu, X., Zadran, H., Moreno, S., Lynch, G., Gall, C., and Bi, X. (2012). Ampakines promote spine actin polymerization, long-term potentiation, and learning in a mouse model of Angelman syndrome. Neurobiol. Dis. *47*, 210–215.

Bedford, M.T., and Richard, S. (2005). Arginine methylation an emerging regulator of protein function. Mol. Cell *18*, 263–272.

Bikkavilli, R.K., and Malbon, C.C. (2011). Arginine methylation of G3BP1 in response to Wnt3a regulates β-catenin mRNA. J. Cell Sci. *124*, 2310–2320.

Blackwell, E., and Ceman, S. (2012). Arginine methylation of RNA-binding proteins regulates cell function and differentiation. Mol. Reprod. Dev. *79*, 163–175.

Blackwell, E., Zhang, X., and Ceman, S. (2010). Arginines of the RGG box regulate FMRP association with polyribosomes and mRNA. Hum. Mol. Genet. *19*, 1314–1323.

Cajigas, I.J., Tushev, G., Will, T.J., tom Dieck, S., Fuerst, N., and Schuman, E.M. (2012). The local transcriptome in the synaptic neuropil revealed by deep sequencing and high-resolution imaging. Neuron *74*, 453–466.

Chadman, K.K., Gong, S., Scattoni, M.L., Boltuck, S.E., Gandhy, S.U., Heintz, N., and Crawley, J.N. (2008). Minimal aberrant behavioral phenotypes of neuroligin-3 R451C knockin mice. Autism Res. *1*, 147–158.

Cheadle, L., and Biederer, T. (2012). The novel synaptogenic protein Farp1 links postsynaptic cytoskeletal dynamics and transsynaptic organization. J. Cell Biol. *199*, 985–1001.

Chen, L.Y., Rex, C.S., Babayan, A.H., Kramár, E.A., Lynch, G., Gall, C.M., and Lauterborn, J.C. (2010). Physiological activation of synaptic Rac>PAK (p-21 activated kinase) signaling is defective in a mouse model of fragile X syndrome. J. Neurosci. *30*, 10977–10984.

Cheng, D., Côté, J., Shaaban, S., and Bedford, M.T. (2007). The arginine methyltransferase CARM1 regulates the coupling of transcription and mRNA processing. Mol. Cell *25*, 71–83.

Côté, J., Boisvert, F.M., Boulanger, M.C., Bedford, M.T., and Richard, S. (2003). Sam68 RNA binding protein is an *in vivo* substrate for protein arginine N-methyltransferase 1. Mol. Biol. Cell *14*, 274–287.

Crawley, J.N. (2007). Mouse behavioral assays relevant to the symptoms of autism. Brain Pathol. *17*, 448–459.

Dansie, L.E., Phommahaxay, K., Okusanya, A.G., Uwadia, J., Huang, M., Rotschafer, S.E., Razak, K.A., Ethell, D.W., and Ethell, I.M. (2013). Long-lasting effects of minocycline on behavior in young but not adult Fragile X mice. Neuroscience *246*, 186–198.

De Rubeis, S., Pasciuto, E., Li, K.W., Fernández, E., Di Marino, D., Buzzi, A., Ostroff, L.E., Klann, E., Zwartkruis, F.J., Komiyama, N.H., et al. (2013). CYFIP1 coordinates mRNA translation and cytoskeleton remodeling to ensure proper dendritic spine formation. Neuron *79*, 1169–1182.

Deng, X., Gu, L., Liu, C., Lu, T., Lu, F., Lu, Z., Cui, P., Pei, Y., Wang, B., Hu, S., and Cao, X. (2010). Arginine methylation mediated by the Arabidopsis homolog of PRMT5 is essential for proper pre-mRNA splicing. Proc. Natl. Acad. Sci. USA *107*, 19114–19119.

Dictenberg, J.B., Swanger, S.A., Antar, L.N., Singer, R.H., and Bassell, G.J. (2008). A direct role for FMRP in activity-dependent dendritic mRNA transport links filopodial-spine morphogenesis to fragile X syndrome. Dev. Cell *14*, 926–939.

Dolzhanskaya, N., Merz, G., Aletta, J.M., and Denman, R.B. (2006). Methylation regulates the intracellular protein-protein and protein-RNA interactions of FMRP. J. Cell Sci. *119*, 1933–1946.

Duffney, L.J., Zhong, P., Wei, J., Matas, E., Cheng, J., Qin, L., Ma, K., Dietz, D.M., Kajiwara, Y., Buxbaum, J.D., and Yan, Z. (2015). Autism-like Deficits in Shank3-Deficient Mice Are Rescued by Targeting Actin Regulators. Cell Rep. *11*, 1400–1413.

Ebrahimi, S., and Okabe, S. (2014). Structural dynamics of dendritic spines: molecular composition, geometry and functional regulation. Biochim. Biophys. Acta *1838*, 2391–2398.

El Fatimy, R., Tremblay, S., Dury, A.Y., Solomon, S., De Koninck, P., Schrader, J.W., and Khandjian, E.W. (2012). Fragile X mental retardation protein interacts with the RNA-binding protein Caprin1 in neuronal RiboNucleoProtein complexes [corrected]. PLoS ONE *7*, e39338.

Feng, J., Yan, Z., Ferreira, A., Tomizawa, K., Liauw, J.A., Zhuo, M., Allen, P.B., Ouimet, C.C., and Greengard, P. (2000). Spinophilin regulates the formation and function of dendritic spines. Proc. Natl. Acad. Sci. USA *97*, 9287–9292.

Feng, Y., Xie, N., Jin, M., Stahley, M.R., Stivers, J.T., and Zheng, Y.G. (2011). A transient kinetic analysis of PRMT1 catalysis. Biochemistry *50*, 7033–7044.

Feuge, J., Scharkowski, F., Michaelsen-Preusse, K., and Korte, M. (2019). FMRP Modulates Activity-Dependent Spine Plasticity by Binding Cofilin1 mRNA and Regulating Localization and Local Translation. Cereb. Cortex *29*, 5204–5216.

Fiala, J.C., Feinberg, M., Popov, V., and Harris, K.M. (1998). Synaptogenesis via dendritic filopodia in developing hippocampal area CA1. J. Neurosci. *18*, 8900–8911.

Fortin, D.A., Srivastava, T., and Soderling, T.R. (2012). Structural modulation of dendritic spines during synaptic plasticity. Neuroscientist *18*, 326–341.

George, J., Soares, C., Montersino, A., Beique, J.C., and Thomas, G.M. (2015). Palmitoylation of LIM Kinase-1 ensures spine-specific actin polymerization and morphological plasticity. eLife *4*, e06327.

Goetze, B., Tuebing, F., Xie, Y., Dorostkar, M.M., Thomas, S., Pehl, U., Boehm, S., Macchi, P., and Kiebler, M.A. (2006). The brain-specific double-stranded RNA-binding protein Staufen2 is required for dendritic spine morphogenesis. J. Cell Biol. *172*, 221–231.

Gokhale, A., Hartwig, C., Freeman, A.H., Das, R., Zlatic, S.A., Vistein, R., Burch, A., Carrot, G., Lewis, A.F., Nelms, S., et al. (2016). The Proteome of BLOC-1 Genetic Defects Identifies the Arp2/3 Actin Polymerization Complex to Function Downstream of the Schizophrenia Susceptibility Factor Dysbindin at the Synapse. J. Neurosci. *36*, 12393–12411.

Guo, A., Gu, H., Zhou, J., Mulhern, D., Wang, Y., Lee, K.A., Yang, V., Aguiar, M., Kornhauser, J., Jia, X., et al. (2014). Immunoaffinity enrichment and mass spectrometry analysis of protein methylation. Mol. Cell. Proteomics *13*, 372–387.

Harris, K.M., Jensen, F.E., and Tsao, B. (1992). Three-dimensional structure of dendritic spines and synapses in rat hippocampus (CA1) at postnatal day 15 and adult ages: implications for the maturation of synaptic physiology and long-term potentiation. J. Neurosci. *12*, 2685–2705.

Honkura, N., Matsuzaki, M., Noguchi, J., Ellis-Davies, G.C., and Kasai, H. (2008). The subspine organization of actin fibers regulates the structure and plasticity of dendritic spines. Neuron *57*, 719–729.

Hotulainen, P., and Hoogenraad, C.C. (2010). Actin in dendritic spines: connecting dynamics to function. J. Cell Biol. *189*, 619–629.

Hotulainen, P., Llano, O., Smirnov, S., Tanhuanpää, K., Faix, J., Rivera, C., and Lappalainen, P. (2009). Defining mechanisms of actin polymerization and depolymerization during dendritic spine morphogenesis. J. Cell Biol. *185*, 323–339.

Hou, L., Antion, M.D., Hu, D., Spencer, C.M., Paylor, R., and Klann, E. (2006). Dynamic translational and proteasomal regulation of fragile X mental retardation protein controls mGluR-dependent long-term depression. Neuron *51*, 441–454.

Hou, W., Nemitz, S., Schopper, S., Nielsen, M.L., Kessels, M.M., and Qualmann, B. (2018). Arginine Methylation by PRMT2 Controls the Functions of the Actin Nucleator Cobl. Dev. Cell *45*, 262–275.e8.

Huber, K.M., Gallagher, S.M., Warren, S.T., and Bear, M.F. (2002). Altered synaptic plasticity in a mouse model of fragile X mental retardation. Proc. Natl. Acad. Sci. USA *99*, 7746–7750.

Hutsler, J.J., and Zhang, H. (2010). Increased dendritic spine densities on cortical projection neurons in autism spectrum disorders. Brain Res. *1309*, 83–94.

Iberg, A.N., Espejo, A., Cheng, D., Kim, D., Michaud-Levesque, J., Richard, S., and Bedford, M.T. (2008). Arginine methylation of the histone H3 tail impedes effector binding. J. Biol. Chem. *283*, 3006–3010.

Irwin, S.A., Galvez, R., and Greenough, W.T. (2000). Dendritic spine structural anomalies in fragile-X mental retardation syndrome. Cereb. Cortex *10*, 1038–1044.

Irwin, S.A., Patel, B., Idupulapati, M., Harris, J.B., Crisostomo, R.A., Larsen, B.P., Kooy, F., Willems, P.J., Cras, P., Kozlowski, P.B., et al. (2001). Abnormal dendritic spine characteristics in the temporal and visual cortices of patients with fragile-X syndrome: a quantitative examination. Am. J. Med. Genet. *98*, 161–167.

Kashima, R., Roy, S., Ascano, M., Martinez-Cerdeno, V., Ariza-Torres, J., Kim, S., Louie, J., Lu, Y., Leyton, P., Bloch, K.D., et al. (2016). Augmented noncanonical BMP type II receptor signaling mediates the synaptic abnormality of fragile X syndrome. Sci. Signal. *9*, ra58.

Kim, S.S., Wang, H., Li, X.Y., Chen, T., Mercaldo, V., Descalzi, G., Wu, L.J., and Zhuo, M. (2011). Neurabin in the anterior cingulate cortex regulates anxiety-like behavior in adult mice. Mol. Brain *4*, 6.

Kim, J.D., Park, K.E., Ishida, J., Kako, K., Hamada, J., Kani, S., Takeuchi, M., Namiki, K., Fukui, H., Fukuhara, S., et al. (2015). PRMT8 as a phospholipase regulates Purkinje cell dendritic arborization and motor coordination. Sci. Adv. *1*, e1500615.

Klein, M.E., Younts, T.J., Castillo, P.E., and Jordan, B.A. (2013). RNA-binding protein Sam68 controls synapse number and local β-actin mRNA metabolism in dendrites. Proc. Natl. Acad. Sci. USA *110*, 3125–3130.

Korobova, F., and Svitkina, T. (2010). Molecular architecture of synaptic actin cytoskeleton in hippocampal neurons reveals a mechanism of dendritic spine morphogenesis. Mol. Biol. Cell *21*, 165–176.

Koskinen, M., Bertling, E., Hotulainen, R., Tanhuanpää, K., and Hotulainen, P. (2014). Myosin IIb controls actin dynamics underlying the dendritic spine maturation. Mol. Cell. Neurosci. *61*, 56–64.

Lai, K.O., and Ip, N.Y. (2013). Structural plasticity of dendritic spines: the underlying mechanisms and its dysregulation in brain disorders. Biochim. Biophys. Acta *1832*, 2257–2263.

Lai, K.O., Wong, A.S., Cheung, M.C., Xu, P., Liang, Z., Lok, K.C., Xie, H., Palko, M.E., Yung, W.H., Tessarollo, L., et al. (2012). TrkB phosphorylation by Cdk5 is required for activity-dependent structural plasticity and spatial memory. Nat. Neurosci. *15*, 1506–1515.

Lee, J., Sayegh, J., Daniel, J., Clarke, S., and Bedford, M.T. (2005). PRMT8, a new membrane-bound tissue-specific member of the protein arginine methyltransferase family. J. Biol. Chem. *280*, 32890–32896.

Lee, P.K.M., Goh, W.W.B., and Sng, J.C.G. (2017). Network-based characterization of the synaptic proteome reveals that removal of epigenetic regulator Prmt8 restricts proteins associated with synaptic maturation. J. Neurochem. *140*, 613–628.

Leung, C., Cao, F., Nguyen, R., Joshi, K., Aqrabawi, A.J., Xia, S., Cortez, M.A., Snead, O.C., 3rd, Kim, J.C., and Jia, Z. (2018). Activation of Entorhinal Cortical Projections to the Dentate Gyrus Underlies Social Memory Retrieval. Cell Rep. *23*, 2379–2391.

Lin, L., Lo, L.H.Y., Lyu, Q., and Lai, K.O. (2017). Determination of dendritic spine morphology by the striatin scaffold protein STRN4 through interaction with the phosphatase PP2A. J. Biol. Chem. *292*, 9451–9464.

Lin, L., Lyu, Q., Kwan, P.Y., Zhao, J., Fan, R., Chai, A., Lai, C.S.W., Chan, Y.S., Shen, X., and Lai, K.O. (2020). The epilepsy and intellectual disability-associated protein TBC1D24 regulates the maintenance of excitatory synapses and animal behaviors. PLoS Genet. *16*, e1008587.

Martin, S., Zekri, L., Metz, A., Maurice, T., Chebli, K., Vignes, M., and Tazi, J. (2013). Deficiency of G3BP1, the stress granules assembly factor, results in abnormal synaptic plasticity and calcium homeostasis in neurons. J. Neurochem. *125*, 175–184.

McFarlane, H.G., Kusek, G.K., Yang, M., Phoenix, J.L., Bolivar, V.J., and Crawley, J.N. (2008). Autism-like behavioral phenotypes in BTBR T+tf/J mice. Genes Brain Behav. *7*, 152–163.

McKinney, R.A. (2010). Excitatory amino acid involvement in dendritic spine formation, maintenance and remodelling. J. Physiol. *588*, 107–116.

Michaelsen-Preusse, K., Zessin, S., Grigoryan, G., Scharkowski, F., Feuge, J., Remus, A., and Korte, M. (2016). Neuronal profilins in health and disease: Relevance for spine plasticity and Fragile X syndrome. Proc. Natl. Acad. Sci. USA *113*, 3365–3370.

Moy, S.S., Nadler, J.J., Young, N.B., Nonneman, R.J., Segall, S.K., Andrade, G.M., Crawley, J.N., and Magnuson, T.R. (2008). Social approach and repetitive behavior in eleven inbred mouse strains. Behav. Brain Res. *191*, 118–129.

Muddashetty, R.S., Nalavadi, V.C., Gross, C., Yao, X., Xing, L., Laur, O., Warren, S.T., and Bassell, G.J. (2011). Reversible inhibition of PSD-95 mRNA translation by miR-125a, FMRP phosphorylation, and mGluR signaling. Mol. Cell *42*, 673–688.

Napoli, I., Mercaldo, V., Boyl, P.P., Eleuteri, B., Zalfa, F., De Rubeis, S., Di Marino, D., Mohr, E., Massimi, M., Falconi, M., et al. (2008). The fragile X syndrome protein represses activity-dependent translation through CYFIP1, a new 4E-BP. Cell *134*, 1042–1054.

Nimchinsky, E.A., Sabatini, B.L., and Svoboda, K. (2002). Structure and Function of Dendritic Spines. Annu. Ren. Physiol. *64*, 313–353.

Njoo, C., Agarwal, N., Lutz, B., and Kuner, R. (2015). The cannabinoid receptor CB1 interacts with the WAVE1 complex and plays a role in actin dynamics and structural plasticity in neurons. PLoS Biol. *13*, e1002286.

Ong, S.E., Mittler, G., and Mann, M. (2004). Identifying and quantifying *in vivo* methylation sites by heavy methyl SILAC. Nat. Methods *1*, 119–126.

Ortega, A.D., Willers, I.M., Sala, S., and Cuezva, J.M. (2010). Human G3BP1 interacts with beta-F1-ATPase mRNA and inhibits its translation. J. Cell Sci. *123*, 2685–2696.

Paik, W.K., Paik, D.C., and Kim, S. (2007). Historical review: the field of protein methylation. Trends Biochem. Sci. *32*, 146–152.

Panas, M.D., Ivanov, P., and Anderson, P. (2016). Mechanistic insights into mammalian stress granule dynamics. J. Cell Biol. *215*, 313–323.

Papa, M., Bundman, M.C., Greenberger, V., and Segal, M. (1995). Morphological analysis of dendritic spine development in primary cultures of hippocampal neurons. J. Neurosci. *15*, 1–11.

Park, S.W., Jun, Y.W., Choi, H.E., Lee, J.A., and Jang, D.J. (2019). Deciphering the molecular mechanisms underlying the plasma membrane targeting of PRMT8. BMB Rep. *52*, 601–606.

Penney, J., Seo, J., Kritskiy, O., Elmsaouri, S., Gao, F., Pao, P.C., Su, S.C., and Tsai, L.H. (2017). Loss of protein arginine methyltransferase 8 alters synapse composition and function, resulting in behavioral defects. J. Neurosci. *37*, 8655–8666.

Penzes, P., Cahill, M.E., Jones, K.A., VanLeeuwen, J.-E., and Woolfrey, K.M. (2011). Dendritic spine pathology in neuropsychiatric disorders. Nat. Neurosci. *14*, 285–293.

Phillips, M., and Pozzo-Miller, L. (2015). Dendritic spine dysgenesis in autism related disorders. Neurosci. Lett. *601*, 30–40.

Pyronneau, A., He, Q., Hwang, J.-Y., Porch, M., Contractor, A., and Zukin, R.S. (2017). Aberrant Rac1-cofilin signaling mediates defects in dendritic spines, synaptic function, and sensory perception in fragile X syndrome. Sci. Signal. *10*, 0852.

Rajyaguru, P., and Parker, R. (2012). RGG motif proteins: modulators of mRNA functional states. Cell Cycle *11*, 2594–2599.

Rex, C.S., Gavin, C.F., Rubio, M.D., Kramar, E.A., Chen, L.Y., Jia, Y., Huganir, R.L., Muzyczka, N., Gall, C.M., Miller, C.A., et al. (2010). Myosin IIb regulates actin dynamics during synaptic plasticity and memory formation. Neuron *67*, 603–617.

Rocca, D.L., Amici, M., Antoniou, A., Blanco Suarez, E., Halemani, N., Murk, K., McGarvey, J., Jaafari, N., Mellor, J.R., Collingridge, G.L., and Hanley, J.G. (2013). The small GTPase Arf1 modulates Arp2/3-mediated actin polymerization via PICK1 to regulate synaptic plasticity. Neuron *79*, 293–307.

Rudge, S.A., and Wakelam, M.J.O. (2009). Inter-regulatory dynamics of phospholipase D and the actin cytoskeleton. Biochim. Biophys. Acta. *179*, 856–861.

Sahoo, P.K., Lee, S.J., Jaiswal, P.B., Alber, S., Kar, A.N., Miller-Randolph, S., Taylor, E.E., Smith, T., Singh, B., Ho, T.S., et al. (2018). Axonal G3BP1 stress granule protein limits axonal mRNA translation and nerve regeneration. Nat. Commun. *9*, 3358.

Santini, E., Huynh, T.N., Longo, F., Koo, S.Y., Mojica, E., D'Andrea, L., and Klann, E. (2017). Reducing eIF4E-eIF4G interactions restores the balance between protein synthesis and actin dynamics in fragile X syndrome model mice. Sci. Signal. *10*, eaan0665.

Sayegh, J., Webb, K., Cheng, D., Bedford, M.T., and Clarke, S.G. (2007). Regulation of protein arginine methyltransferase 8 (PRMT8) activity by its N-terminal domain. J. Biol. Chem. *282*, 36444–36453.

Segal, M. (2001). Rapid plasticity of dendritic spine: hints to possible functions? Prog. Neurobiol. *63*, 61–70.

Shiina, N. (2019). Liquid- and solid-like RNA granules form through specific scaffold proteins and combine into biphasic granules. J. Biol. Chem. *294*, 3532–3548.

Silverman, J.L., Yang, M., Lord, C., and Crawley, J.N. (2010). Behavioural phenotyping assays for mouse models of autism. Nat. Rev. Neurosci. *11*, 490–502.

Skarnes, W.C., Rosen, B., West, A.P., Koutsourakis, M., Bushell, W., Iyer, V., Mujica, A.O., Thomas, M., Harrow, J., Cox, T., et al. (2011). A conditional knockout resource for the genome-wide study of mouse gene function. Nature *474*, 337–342.

Solomon, S., Xu, Y., Wang, B., David, M.D., Schubert, P., Kennedy, D., and Schrader, J.W. (2007). Distinct structural features of caprin-1 mediate its interaction with G3BP-1 and its induction of phosphorylation of eukaryotic translation initiation factor 2alpha, entry to cytoplasmic stress granules, and selective interaction with a subset of mRNAs. Mol. Cell. Biol. *27*, 2324–2342.

Spence, E.F., Kanak, D.J., Carlson, B.R., and Soderling, S.H. (2016). The Arp2/3 Complex Is Essential for Distinct Stages of Spine Synapse Maturation, Including Synapse Unsilencing. J. Neurosci. *36*, 9696–9709.

Stetler, A., Winograd, C., Sayegh, J., Cheever, A., Patton, E., Zhang, X., Clarke, S., and Ceman, S. (2006). Identification and characterization of the methyl arginines in the fragile X mental retardation protein Fmrp. Hum. Mol. Genet. *15*, 87–96.

Tada, T., Simonetta, A., Batterton, M., Kinoshita, M., Edbauer, D., and Sheng, M. (2007). Role of Septin cytoskeleton in spine morphogenesis and dendrite development in neurons. Curr. Biol. *17*, 1752–1758.

Tong, L., Prieto, G.A., and Cotman, C.W. (2018). IL-1β suppresses cLTP-induced surface expression of GluA1 and actin polymerization via ceramide-mediated Src activation. J. Neuroinflammation *15*, 127.

Tsai, W.C., Gayatri, S., Reineke, L.C., Sbardella, G., Bedford, M.T., and Lloyd, R.E. (2016). Arginine Demethylation of G3BP1 Promotes Stress Granule Assembly. J. Biol. Chem. *291*, 22671–22685.

Vessey, J.P., Macchi, P., Stein, J.M., Mikl, M., Hawker, K.N., Vogelsang, P., Wieczorek, K., Vendra, G., Riefler, J., Tübing, F., et al. (2008). A loss of function allele for murine Staufen1 leads to impairment of dendritic Staufen1-RNP delivery and dendritic spine morphogenesis. Proc. Natl. Acad. Sci. USA *105*, 16374–16379.

Winslow, S., Leandersson, K., and Larsson, C. (2013). Regulation of PMP22 mRNA by G3BP1 affects cell proliferation in breast cancer cells. Mol. Cancer *12*, 156.

Wu, H., Cottingham, C., Chen, L., Wang, H., Che, P., Liu, K., and Wang, Q. (2017). Age-dependent differential regulation of anxiety- and depression-related behaviors by neurabin and spinophilin. PLoS One *12*, e0180638.

Xie, Y., Vessey, J.P., Konecna, A., Dahm, R., Macchi, P., and Kiebler, M.A. (2007). The GTP-binding protein Septin 7 is critical for dendrite branching and dendritic-spine morphology. Curr. Biol. *17*, 1746–1751.

Yadav, S., Oses-Prieto, J.A., Peters, C.J., Zhou, J., Pleasure, S.J., Burlingame, A.L., Jan, L.Y., and Jan, Y.N. (2017). TAOK2 kinase mediates PSD95 stability and dendritic spine maturation through Septin7 phosphorylation. Neuron *93*, 379–393.

Yan, Z., Kim, E., Datta, D., Lewis, D.A., and Soderling, S.H. (2016). Synaptic Actin Dysregulation, a Convergent Mechanism of Mental Disorders? J. Neurosci. *36*, 11411–11417.

Yang, M., Silverman, J.L., and Crawley, J.N. (2011). Automated three-chambered social approach task for mice. Curr. Protoc. Neurosci. *56*, 8.26.1–8.26.16.

Yang, X., Hu, Z., Zhang, Q., Fan, S., Zhong, Y., Guo, D., Qin, Y., and Chen, M. (2019). SG formation relies on eIF4GI-G3BP interaction which is targeted by picornavirus stress antagonists. Cell Discov. *5*, 1.

Yuste, R. (2011). Dendritic spines and distributed circuits. Neuron *71*, 772–781.

Zappulo, A., van den Bruck, D., Ciolli Mattioli, C., Franke, V., Imami, K., McShane, E., Moreno-Estelles, M., Calviello, L., Filipchyk, A., Peguero-Sanchez, E., et al. (2017). RNA localization is a key determinant of neurite-enriched proteome. Nat. Commun. *8*, 583.

Zhao, J., Fok, A.H.K., Fan, R., Kwan, P.Y., Chan, H.L., Lo, L.H., Chan, Y.S., Yung, W.H., Huang, J., Lai, C.S.W., and Lai, K.O. (2020). Specific depletion of the motor protein KIF5B leads to deficits in dendritic transport, synaptic plasticity and memory. eLife *9*, e53456.

Ziv, N.E., and Smith, S.J. (1996). Evidence for a role of dendritic filopodia in synaptogenesis and spine formation. Neuron *17*, 91–102.

STAR★METHODS

KEY RESOURCES TABLE

REAGENT or RESOURCE	SOURCE	IDENTIFIER
Antibodies		
Mouse monoclonal anti-Actin	Sigma-Aldrich	Cat#A3853; RRID: AB_262137
Rabbit monoclonal anti-Asymmetric Di-Methyl Arginine Motif [adme-R] MultiMab	Cell Signaling Technology	Cat#13522; RRID: AB_2665370
Rabbit monoclonal anti-Cofilin	Cell Signaling Technology	Cat#5175; RRID: AB_10622000
Rabbit monoclonal anti-Phospho-Cofilin (Ser3) (77G2)	Cell Signaling Technology	Cat#3313; RRID: AB_2080597
Rabbit monoclonal l anti-eIF4E (C46H6)	Cell Signaling Technology	Cat#2067; RRID: AB_2097675
Rabbit polyclonal anti-eIF4G	Cell Signaling Technology	Cat#2498; RRID: AB_2096025
Mouse monoclonal anti-FLAG® M2	Sigma-Aldrich	Cat#F1804; RRID: AB_262044
Rabbit polyclonal anti-G3BP1 (Western blot, immunoprecipitation)	Bethyl	Cat#A302-033A; RRID: AB_1576539
Rabbit polyclonal anti-G3BP1 (ICC)	Proteintech	Cat#13057-2-AP; RRID: AB_2232034
Rabbit polyclonal anti-G3BP2	Bethyl	Cat#A302-040A; RRID: AB_1576545
Mouse monoclonal Anti-GFP (3E6)	Invitrogen	Cat#A-11120; RRID: AB_221568
Anti-mouse IgG, HRP-linked Antibody	Cell Signaling Technology	Cat#7076; RRID: AB_330924
Anti-rabbit IgG, HRP-linked Antibody	Cell Signaling Technology	Cat#7074; RRID: AB_2099233
Mouse monoclonal Anti-MAP2	Sigma-Aldrich	Cat#M4403; RRID: AB_477193
Rabbit monoclonal anti- Mono-Methyl Arginine (R*GG) (D5A12)	Cell Signaling Technology	Cat#8711; RRID: AB_10896849
Rabbit polyclonal anti-Phospho-PAK1 (Ser199/204)/ PAK2 (Ser192/197)	Cell Signaling Technology	Cat#2605; RRID: AB_2160222
Rabbit polyclonal anti-PAK1	Cell Signaling Technology	Cat#2602; RRID: AB_330222
Rabbit polyclonal anti-PRMT1 (A33)	Cell Signaling Technology	Cat#2449; RRID: AB_2237696
Rabbit polyclonal anti-PRMT3	Thermo Fisher Scientific	Cat#PA5-30363; RRID: AB_2547837
Mouse monoclonal Anti -PRMT4/CARM1 (3H2)	Cell Signaling Technology	Cat#12495; RRID: AB_2797935
Goat polyclonal anti-PRMT5	Santa Cruz Biotechnology	Cat#sc-22132; RRID: AB_2171803
Rabbit polyclonal anti-PRMT6	Abcam	Cat#ab47244; RRID: AB_2284473
Rabbit polyclonal anti-PRMT8 (ICC)	Thermo Fisher Scientific (discontinued)	Cat#PA5-19846; RRID: AB_10985902
Rabbit polyclonal anti-PRMT8 (Western blot)	Abcam (discontinued)	Cat#ab134774
Mouse monoclonal Anti-PSD-95	Thermo Fisher Scientific	Cat#MA1-046; RRID: AB_2092361
Mouse monoclonal Anti-PSD-95	NeuroMab Facility	Cat#75-028; RRID: AB_2292909
Mouse monoclonal Anti-Rac1	Cytoskeleton	Cat#ARC03; RRID: AB_2721173)
Rabbit polyclonal anti-RFP	Rockland	Cat# 600-401-379; RRID: AB_2209751
Rabbit polyclonal anti-RNMT	Millipore	Cat#06-1355; RRID: AB_11215450
Rabbit polyclonal anti-SEPT7	Sigma-Aldrich	Cat#HPA029524; RRID: AB_10601573
Rabbit polyclonal anti-Staufen	Abcam	Cat#ab73478; RRID: AB_1641030
Rabbit anti-VGLUT1	Sigma-Aldrich	Cat#V0389; RRID: AB_261840
Bacterial and Virus Strains		
pAAV-CaMKIIα-eYFP	Karl Deisseroth (Neurosciences Institute of Stanford University)	RRID: Addgene_105622
Biological Samples		
Brain slices (M. musculus)	This paper	N/A
Hippocampus (M. musculus)	This paper	N/A
Primary hippocampal neuron (R. norvegicus and M. musculus)	This paper	N/A
Primary cortical neuron (R. norvegicus and M. musculus)	This paper	N/A

(*Continued on next page*)

Continued

REAGENT or RESOURCE	SOURCE	IDENTIFIER
Synaptoneurosome (M. musculus)	This paper	N/A
Total brain (M. musculus)	This paper	N/A
Chemicals, Peptides, and Recombinant Proteins		
ANTI-FLAG® M2 Affinity Gel	Sigma-Aldrich	Cat#A2220
DAPI Solution	Thermo Fisher Scientific	Cat#62248
FRAX 486	Tocris Bioscience	Cat#5910/10
Immobilized γ-Aminophenyl-m7GTP (C10-spacer)	Jena Bioscience	Cat#AC-155
PAK-PBD Beads	Cytoskeleton	Cat#PAK02-A
nProtein A Sepharose	GE Health	Cat#17-5280-01
Tetrodotoxin citrate	Abcam	Cat#ab120055
Critical Commercial Assays		
Neon™ 100ul Transfection Kit	Thermo Fisher Scientific	Cat#MPK10025
Lipofectamine LTX with Plus Reagent	Thermo Fisher Scientific	Cat#15338100
ViewRNA™ ISH Cell Assay Kit	Thermo Fisher Scientific	Cat#QVC0001
Experimental Models: Organisms/Strains		
Mouse: Strain background: C57BL/6N: *Prmt8*$^{tm1a(EUCOMM)Wtsi}$	Wellcome Sanger Institute EMMA mouse repository	MGI ID:4434085 EM:04479
Oligonucleotides		
Sense probe against rat Prmt8	Affymetrix	GenBank: NM_001271385-N
Antisense probe against rat Prmt8	Affymetrix	GenBank: NM_001271385-N
Control shRNA: 5′-GGCTACCTCCATTTAGTGT-3′	This paper	N/A
G3BP1-shRNA: 5′-CCTGTGTCCGACATTCAAG-3	This paper	N/A
G3BP2-shRNA: 5′-TGCTAACAGCGCTTACTAT-3′	This paper	N/A
Primers, see Table S1	This paper	N/A
PRMT8-shRNA (442): 5′-CTCAGAGAAGATCATTAAG-3′	This paper	N/A
PRMT8-shRNA (1028): 5′-GACTACCTCACTGTTCGAA-3′	This paper	N/A
Synthetic Human PRMT8	Invitrogen	NM_019854.5
Recombinant DNA		
pEGFP-N1	Clontech (discontinued)	N/A
pEGFP-N1-PRMT8	This paper	N/A
pcDNA3-FLAG-G3BP1	This paper	N/A
pcDNA3-FLAG-G3BP1-R433/445H	This paper	N/A
pcDNA3-G3BP1-shRNAir	This paper	N/A
pcDNA3-G3BP1-shRNAir-R433/445H	This paper	N/A
pcDNA3-FLAG-PRMT8	This paper	N/A
pcDNA3-PRMT8	This paper	N/A
pcDNA3-PRMT8-RNAir	This paper	N/A
pcDNA3-PRMT8-RNAir G121A	This paper	N/A
pcDNA3-PRMT8-RNAir K107R	This paper	N/A
pcDNA3-PRMT8-RNAir G2A NLS	This paper	N/A
pcDNA3-PRMT8-GFP G2A NLS	This paper	N/A
pSUPER	Oligoengine	Cat#VEC-PBS-0001/0002
Software and Algorithms		
ANY-maze software	ANY-maze	RRID:SCR_014289
CLC Main Workbench	https://digitalinsights.qiagen.com/products-overview/discovery-insights-portfolio/analysis-and-visualization/qiagen-clc-main-workbench/	RRID:SCR_000354

(*Continued on next page*)

Continued

REAGENT or RESOURCE	SOURCE	IDENTIFIER
GraphPad Prism	https://graphpad.com	RRID:SCR_015807
ImageJ	https://imagej.net	RRID:SCR_003070
MetaMorph software	Molecular Devices	SCR_002368
Mini Analysis Program	http://www.synaptosoft.com/MiniAnalysis	RRID:SCR_002184
Volocity	Quorum Technologies	RRID:SCR_002668
Zen digital imaging software	Zeiss	RRID:SCR_013672
Other		
ImageJ plug-in "JACoP"	https://imagej.nih.gov/ij/plugins/track/jacop.html	N/A

RESOURCE AVAILABILITY

Lead Contact

Further information and requests for resources and reagents should be directed to and will be fulfilled by the Lead Contact, Kwok-On Lai (laiko@hku.hk; laikofmb405@gmail.com).

Materials Availability

All unique/stable reagents generated in this study are available from the Lead Contact with a completed Materials Transfer Agreement.

Data and Code Availability

This study did not generate any unique datasets or code.

EXPERIMENTAL MODEL AND SUBJECT DETAILS

Animals

The mice were handled in a humane manner and group housed in The Laboratory Animal Unit, The University of Hong Kong with food and water under a 12-hour light/dark cycle, accredited by Association for Assessment and Accreditation of Laboratory Animal Care International. All animal experiments were approved and performed in accordance with University of Hong Kong Committee on the Use of Live Animals in Teaching and Research guidelines. The *Prmt8* knockout mouse line with the *Prmt8*$^{tm1a(EUCOMM)Wtsi}$ allele was generated by Wellcome Sanger Institute (the European Conditional Mouse Mutagenesis Program and Knockout Mouse Project and Sanger Mouse Genetics Project). The methods of mouse line generation and genotyping were described previously (Kim et al., 2015). Mice were in the C57BL/6N background. Three to four weeks old mice of both genders were used for western blot analysis, confocal imaging and behavioral testing. ICR mouse embryos of both genders were used for in utero electroportation at embryonic day 15. To prepare primary cortical and hippocampal neurons, day 18 embryos of both genders from Sprague Dawley rats were used.

Primary neuronal culture

Primary hippocampal and cortical neurons were dissociated from day 18 embryos of Sprague Dawley rats. Hippocampal neurons were cultured on 18-mm coverslips coated with poly-D-lysine (1 mg/ml, Sigma). High density neurons (1.4×10^5 cells per coverslip) were used for dendritic spine analysis, while low density neurons (0.4×10^5 cells per coverslip) were used for immunofluorescence staining. Hippocampal neurons were cultured on 35-mm tissue cultre dishes or 35-mm MatTek dishes with central cover glass (MatTek corp) coated with poly-D-lysine (0.1 mg/ml for 35-mm dish and 1 mg/ml for MatTek dish), with a density of 1×10^6 cells per 35-mm dish (for western blot analysis) or 2×10^5 cells per MatTek dish (for live cell imaging). The neurons were grown in 37°C, 5% CO_2 with Neurobasal medium supplemented with 2% B27 and 0.25% L-glutamine (Invitrogen).

Cortical neurons were cultured on 35-mm dishes coated with poly-D-lysine (Sigma, 0.1 mg/ml) with a density of 1×10^6 cells per dish. The neurons were cultured in 37°C, 5% CO_2 with Neurobasal medium supplemented with 2% B27 and 0.5% L-glutamine (Invitrogen).

METHOD DETAILS

DNA constructs

To knock down PRMT8, G3BP1 or G3BP2, the 19-nucleotides shRNA derived from rat PRMT8, rat G3BP1 or rat G3BP2 nucleotide sequence were selected by the online siRNA design program (http://sirna.wi.mit.edu) and were used to create the shRNA after subcloning into the pSUPER vector.

All expression constructs were made by PCR using high-fidelity Pfu DNA polymerase (Agilent Technologies, Inc.). The sequences of all primers were listed in Table S1. The PCR products were digested by EcoRI (NEB) and KpnI (NEB) and subcloned into the pcDNA3 vector. For making FLAG-tagged PRMT8, the PRMT8 insert was amplified from synthetic full length human PRMT8 by PCR. For making FLAG-tagged G3BP1, the G3BP1 insert was amplified from rat hippocampus cDNA. For making the GFP-tagged PRMT8 construct, the PCR product was digested by EcoRI and KpnI and sub-cloned into the pEGFP-N1 vector. To make RNAi-resistant constructs and different variants [methyltransferase-deficient G121A-PRMT8, phospholipase D-deficient K107R-PRMT8, nuclear-restricted PRMT8 with the G2A mutation and addition of the NLS, G3BP1 methylation-deficient constructs (R433/445H)], constructs were created by site-directed mutagenesis using PfuUltra II Fusion HS DNA Polymerase (Agilent), and the PCR products were digested by DpnI (NEB) at 37°C for 3 hours before transformation into *E. coli* competent cells. The pAAV-CaMKIIα-eYFP construct was packaged into AAV5 capsid particles by UNC Vector Core. Sterile artificial cerebrospinal fluid was used to dilute AAV5 viruses for injection. The nucleotide sequence of the insert in each plasmid construct was verified by Sanger sequencing.

Transfection of primary neurons

Neurons were transfected with different plasmids using calcium phosphate precipitation as previously described (Lai et al., 2012). To test knockdown efficiency by western blot, control shRNA or PRMT8 shRNA was transfected into primary cortical neurons by electroporation using the Neon^{TM} transfection system (Invitrogen). Cortical neurons (1×10^6) in suspension were electroporated in each reaction using 1600 V pulse voltage and 20 ms pulse width. Immediately after electroporation, cells were seeded onto PDL-coated 35mm dishes and cultured for 5 days before western blot analysis.

Preparation of synaptoneurosome (SNS)

Mouse cortices were obtained from C57BL/6N mice at postnatal day 15-16. The cortices were homogenized manually with Potter-Elvehjem Tissue Grinder and Fluoropolymer Resin Pestle (Corning) in homogenization buffer (0.12 M NaCl, 4.7 mM KCl, 1.2 mM $MgSO_4.7H_2O$, 2.5 mM $CaCl_2.2H_2O$, 1.53 mM KH_2PO_4, 212.7 mM D-glucose in DEPC-H_2O) with various protease and phosphatase inhibitors (10 μg/ml soybean trypsin inhibitor, 10 μg/ml leupeptin, 10 μg/ml aprotinin, 2 μg/ml antipain, 30 nM okadaic acid, 5 mM benzamidine, 1 mM sodium orthovanadate, 1 mM PMSF, 1 mM sodium fluoride, 100 mM beta-glycerophosphate) and centrifuged at 4°C, 2 minutes, 2000 g. The supernatant was collected and some was saved as the homogenate (Homo) fraction. The rest of the lysate was filtered by 100 μm and then 10 μm nylon net filters (Millipore). The filtrate was centrifuged at 4°C, 15 minutes, 1000 g, and the supernatant was saved. The pellet was resuspended in homogenization buffer and saved as the SNS fraction. The different fractions were then analyzed by western blot.

Pharmacological treatment of neurons and western blot analysis

To examine the effect of PAK inhibition on dendritic spine morphology, cultured hippocampal neurons were transfected at 13 DIV. Cells were treated with 500 nM FRAX486 (Tocris) or dimethyl sulfoxide (Sigma) in incubator (37°C, 5% CO_2) for 2 hours at 16 DIV. To examine the dependence of PRMT8 protein expression on neuronal activity, hippocampal neurons at 16 DIV were treated with TTX (2 μM) for 48 hours before cell lysis.

To determine the temporal expression of PRMT8 along development, hippocampi on postnatal day 1, 7, 14, 21, 31 and 56 were collected in cold RIPA lysis buffer (0.5% sodium deoxycholate, 1% NP-40, 0.1% SDS in D-PBS) containing various protease and phosphatase inhibitors (10 μg/ml soybean trypsin inhibitor, 10 μg/ml leupeptin, 10 μg/ml aprotinin, 2 μg/ml antipain, 30 nM okadaic acid, 5 mM benzamidine, 1 mM sodium orthovanadate, 1 mM PMSF, 1 mM sodium fluoride, 100 mM beta-glycerophosphate). Primary hippocampal neurons cultured on 3, 7, 10, 14 and 21 DIV were lysed by RIPA buffer containing protease and phosphatase inhibitors. The lysate was rocked at 4°C for 45 minutes before centrifugation at 4°C, for 10 minutes at 13000 rpm. 1X Sample buffer (5X sample buffer: 300 mM Tris-HCl buffer pH 6.8, 10% (w/v) SDS, 25% (v/v) beta-mercaptoethanol, 50% (v/v) glycerol, 0.05% (w/v) bromophenol blue) was added to the protein extract and boiled for 6 minutes. The protein samples were separated by SDS-PAGE and transferred onto PVDF membrane. The membrane was blocked in 5% non-fat milk in TBS with 0.1% Tween 20 (TBST) at room temperature for 1 hour with rocking. The membrane was then incubated in primary antibody (PRMT8: Abcam, 1:1000) diluted in 5% BSA at 4°C overnight. After washing with TBST for 3 times, the membrane was incubated in Horseradish peroxidase-conjugated secondary antibody (1:3000) diluted in 5% non-fat milk in TBST at room temperature for 1 hour with rocking. The signal was detected by ECL (Thermo Scientific) and the intensity quantified by the Photoshop software.

Immunoprecpitation and pull-down assay

HEK293T cells were grown to 70%–80% confluence and transfected with FLAG-PRMT8 or FLAG-G3BP1 using Lipofectamine plus reagent according to manufacturer's protocol (Invitrogen). Cell lysate was collected using RIPA lysis buffer 1 day post-transfection. Lysate (0.5 mg) was incubated with FLAG beads (15 μl, Sigma) for 2 hours at 4°C to immunoprecipitate the FLAG-tagged proteins. After washing three times by RIPA, proteins were eluted with 2X sample buffer for western blot analysis. For pull-down assay, brain lysate or SNS was prepared by NP-40 lysis buffer [50 mM tris buffer (pH 8.5), 50 mM NaCl, 0.5% NP-40 in MIliQ H_2O], and 1 mg brain lysate or SNS was incubated with FLAG beads containing G3BP1 or PRMT8 overnight at 4°C. After washing the beads three times by NP-40 lysis buffer, proteins were eluted with 2X sample buffer for western blot analysis.

Rac1 activity assay and the m^7GTP pull-down assays were performed as described previously (Santini et al., 2017). Mouse brains were homogenized with lysis buffer [150 mM NaCl, 10 mM $MgCl_2$, 30 mM tris buffer (pH 8.0), 1 mM DTT, 1.5% Triton X-100 and protease inhibitors]. Lysate (0.5 to 1 mg) was incubated with PAK-PBD beads (20 μl, Cytoskeleton) or m^7GTP beads (20 μl, Jena Bioscience) for 2 hours at 4°C with rotation. The beads were centrifuged for 1 min at 6,000 rpm and washed with 600 μL washing buffer [100 mM KCl, 50 mM tris buffer (pH 7.4), 5 mM MgCl 2, 0.5% Triton X-100] for three times. After washing, the beads were eluted with 2X Sample buffer for western blot analysis.

To detect asymmetric dimethylation of G3BP1, mouse SNS (1 mg) was incubated with G3BP1 antibody (1 μg) overnight at 4°C. After incubation with proteins A beads (40 μl, GE Healthcare) at 4°C for 1 hour, the beads were washed three times with RIPA and proteins were eluted with 2X Sample buffer for western blot analysis.

F-actin/G-actin ratio

F-actin/G-actin assay was performed as previously described (Pyronneau et al., 2017). Primary cortical neurons (14 DIV) cultured from wild-type or *Prmt8* knockout mice were collected in G-actin soluble lysis buffer [10 mM K_2HPO_4, 100 mM NaF, 50 mM KCl, 2 mM $MgCl_2$, 1 mM EGTA, 0.2 mM DTT, 1 mM sucrose (pH 7.0), 0.5% Triton X-100], followed by centrifugation at 13,000 rpm for 30 min. The supernatant was transferred to a new tube and saved (G-actin). The remaining pellet (F-actin) was resuspended in buffer containing equal volume of lysis buffer and a second buffer [1.5 mM guanidine hydrochloride, 1 mM sodium acetate, 1 mM $CaCl_2$, 1 mM ATP, 20 mM Tris-HCl (pH 7.5)] and rotated at 4°C for 1 hour, followed by centrifugation at 13,000 rpm for 30 min. The supernatant was transferred to a new tube (F-actin). Equal volumes of F-actin and G-actin samples were loaded for western blotting.

In situ hybridization

The localization of *Prmt8* mRNA in hippocampal neuron was examined by the ViewRNA ISH Cell Assay kit (Thermo Scientific). Sense and antisense probes were designed against rat *Prmt8* by Affymetrix. The *in situ* hybridization was performed as described in our previous study (Zhao et al., 2020) with some modifications from the manufacturer instruction. The protease QS treatment was skipped as several protein markers needed to be preserved for the subsequent immunofluorescence staining. After *in situ* hybridization, cells were washed by D-PBS and incubated with blocking buffer (10% goat serum in D-PBS) for 30 minutes. The cells were then incubated with MAP2 antibody (1:500) diluted in blocking buffer at 4°C. On the next day after washing with D-PBS for 3 times, the cells were incubated with Alexa-conjugated secondary antibody (1:1000) diluted in blocking buffer for 1 hour. The cells were then washed with D-PBS for 3 times and incubated with DAPI (1:100) diluted in D-PBS at room temperature for 5 minutes. The cells were washed with D-PBS for 3 times before mounting on slide with gold antifade reagent (Life Technologies).

In utero electroporation, stereotaxic injection, perfusion and brain sectioning

Control shRNA or PRMT8 shRNA with tdTomato vector (0.8 μg control shRNA or PRMT8 shRNA with 0.4 μg tdTomato vector) and blue visible dye was injected to the right ventricle of ICR mouse embryos (day 15). Plasmids were taken up into the hippocampus by electroporation with a 5-mm platinum plated electrode (Brand: BTX) and electro square porator (Brand: BTX) at 28V, 5 pulses. At postnatal day 21, the pups were perfused by 4% paraformaldehyde (PFA) and the brains were post-fixed in cold 4% PFA for 48 hours. To investigate the spine morphology of *Prmt8* knockout mice, AAV5 carrying YFP-expressing construct was stereotaxically injected into the hippocampi of 6-week-old wild-type and *Prmt8* homozygous knockout mice as described in our previous study (Lin et al., 2020). Two weeks after surgery, the mice were perfused by 4% PFA and the brains were post-fixed in cold 4% PFA for 48 hours. All fixed mouse brains were coronally sectioned at 50 μm on Vibratome (Leica).

Immunofluorescence staining, confocal imaging and quantitative analysis

Primary hippocampal neurons were fixed by 4% PFA/4% sucrose in PBS at room temperature for 15 minutes. The cells were washed by D-PBS for 3 times followed by incubation with blocking medium [0.4% Triton X-100 (vol/vol) and 1% BSA (vol/vol)] at room temperature for 45 minutes. The cells were then incubated with primary antibody diluted in blocking medium at 4°C overnight. On the next day after washing 3 times in washing buffer (0.02% Triton X-100 and 0.25% BSA in D-PBS), cells were incubated with Alexa-conjugated secondary antibody diluted in incubation buffer (0.02% Triton X-100 and 1% BSA in D-PBS) at room temperature for 1 hour. The cells were washed two times with washing buffer, once with D-PBS and rinsed twice with filtered milliQ water before mounting on slide with hydromount medium (National Diagnostics). For GFP staining of neurons, cells were incubated with GFP antibody (1:2000) diluted in GDB buffer at 4°C overnight after fixing. On the next day after washing 3 times with filtered phosphate buffer (20 mM phosphate buffer and 0.5 M NaCl), cells were incubated with Alexa 488 conjugated secondary antibody (1:2000) diluted in GDB buffer at room temperature for 1 hour. The cells were then washed with filtered phosphate buffer for 3 times, once with D-PBS and rinsed twice with filtered milliQ water before mounting on slide with hydromount medium.

Brain slices were washed by D-PBS for 3 times followed by incubation with blocking medium (0.3% Triton X-100 and 1.5% normal goat serum in D-PBS) at room temperature for 1 hour with rocking. The slices were then incubated with primary antibody diluted in blocking medium at 4°C for 48 hours with rocking. After washing with D-PBS for 3 times, slices were incubated with Alexa-conjugated secondary antibody at room temperature for 2 hours with rocking. The slices were washed three times with D-PBS and mounted on slide with hydromount medium.

Olympus Fluoview 300, Carl Zeiss LSM 700, 780 and 800 (with airyscan mode) confocal microscopes with Zen digital imaging software were used for fluorescence image acquisition. To study the subcellular localization of PRMT8 and PSD-95, Olympus Fluoview 300 was used to acquire the Z stack images using the 60x oil-immersion objective with 0.5x optical zoom. For *in situ* hybridization, LSM 780 was used to acquire the Z stack images using the 40x oil-immersion objective at a resolution of 1024 × 1024 pixels with the following parameters: 1x optical zoom, averaged 2 times, scan speed 7, 0.40 μm interval with 16-bit dynamic of range, 1 AU of pinhole for each channel. For imaging the localization of GFP-tagged PRMT8, analysis of dendritic spines of primary hippocampal neurons and CA1 hippocampal neurons in brain slices of mice after *in utero* electroporation, LSM 700 was used to acquire the images using the 63x oil-immersion objective at a resolution of 1024 × 1024 pixels with the following parameters: 0.5x optical zoom, averaged 2 times, scan speed 7-8, 0.40 μm interval with 16-bit dynamic of range, 1 AU of pinhole for each channel. Images of secondary apical dendrites of CA1 hippocampal neurons in brain slices were captured. For imaging the vGLUT1 and PSD-95 juxtaposed puncta in cultured hippocampal neuron and spines of secondary apical dendrites of CA1 hippocampal neurons in *Prmt8* knockout brain slices, LSM 800 was used to acquire the Z stacked images using the 63x oil-immersion objective at a resolution of 1024 × 1024 pixels with the following parameters: 1.6x optical zoom, averaged 2 times, scan speed 4, 0.35 μm interval with 16-bit dynamic of range, 1 AU of pinhole for each channel. All the channels remained the same in parameter settings throughout the image acquisition for each batch of experiment, except for the MAP2, GFP or RFP staining to which the laser power and optical gain were slightly adjusted in different cells. The dendritic spine morphology was quantified and analyzed by the MetaMorph software.

The morphology of dendritic spines was classified based on our previous study (Lin et al., 2017). The spines were classified into mushroom spine, stubby spine, thin spine or filopodium according to the ratio of length (L), head width (H) and neck width (N): mushroom spine was defined as those having the ratio of $H/N \geq 1.5$. Stubby spines were defined as those with $H/N \leq 1$ and $L/N \leq 1$; thin spines had the ratio of $1 \leq H/N < 1.5$ and $1.5 \leq L/N \leq 3$. Filopodia were defined as those with the ratio of $H/N < 1.2$ and $L/N > 3$.

To analyze the degree of overlap between PRMT8 and PSD-95, PRMT8 and phalloidin, as well as PRMT8 and G3BP1, ImageJ software with the plug-in "JACoP" was used for the analysis of Pearson's correlation. Pearson's correlation with a range from −1 to 1: −1 stands for perfect exclusion, 0 means random localization and 1 represents perfect correlation. For the quantification of puncta number, threshold was set on the images by the ImageJ software to define puncta that have three-fold higher intensity than that on the adjacent dendritic shaft. The total number of threshold puncta as well as the number of puncta that showed overlap of the two channels was then calculated manually.

Calcium imaging of hippocampal neuron

To capture the GCaMP6 calcium transient events, the transfected neurons were first treated with TTX (1 μM) in imaging buffer (125 mM NaCl, 5 mM KCl, 10 mM HEPES, 2 mM $CaCl_2$, 1 mM $MgCl_2$, 10 mM glucose in milliQ water, pH7.2) for 10 minutes in 37°C, 5% CO_2, followed by treatment with imaging buffer without $MgCl_2$ for 5 minutes in 37°C, 5% CO_2. Live imaging of dendrites was taken using Perkin Elmer UltraView Vox Spinning Disk Confocal Microscope with 100x oil-immersion objective at a resolution of 512 × 512 pixels, 3 frames per second for 10 minutes. Images were exported using Volocity software. For monitoring the movement of PRMT8 to actin polymerization sites on dendritic spines, live imaging of dendrites was taken using Perkin Elmer UltraView Vox Spinning Disk Confocal Microscope with 60x oil-immersion objective at a resolution of 512 × 512 pixels, 1.2 frames per second for 100 frames.

FRAP experiments

FRAP experiments were performed as previously described (Koskinen et al., 2014; George et al., 2015). Briefly, hippocampal neurons (14DIV) were cotransfected with GFP, mCherry-LifeAct and different constructs of interest. Images of dendritic spines (17DIV) were acquired for both mCherry and GFP signals by Perkin Elmer UltraView Vox Spinning Disk Confocal Microscope with 60x oil-immersion objective at a resolution of 512 × 512 pixels. The frame was imaged three times at 2 s intevals before photobleaching. FRAP was performed only on the mCherry-LifeAct channel of a region of interest (a single spine) by scanning with the 561 nm laser line at 100% laser power (UltraVIEW PK cycles: 500, spot period: 3000 ms, spot cycle: 5000). Imaging of the frame was resumed immediately after the completion of the photobleaching and continued every 0.8-2 s for approximately 120 s.

The ROI mCherry-LifeAct intensity was measured by ImageJ. We subtracted any remaining signal at the first post-bleach time point, and renormalized this data to baseline (pre-bleach measurements) after setting the point as 0, as described previously (George et al., 2015). For the quantification of mCherry-LifeAct mobile fraction, we used a previously described method (Honkura et al., 2008; Koskinen et al., 2014; George et al., 2015). After plotting the normalized FRAP values of each group, a linear regression in the region exceeding $\sim 5 \times t_{1/2}$ was made. The y-intercept value was defined as the dynamic fraction. To determine $t_{1/2}$, a nonlinear regression was performed in GraphPad Prism by fitting data to the equation: Y = Y0 + (Plateau-Y0)*(1-exp(-K*x)). Y_0 is the fluorescence value immediately post-bleach, Plateau is the y value at infinite times. K is the rate constant and $t_{1/2}$ is computed as ln(2)/K.

Electrophysiology

Whole cell recordings were obtained from hippocampal neurons at 17-18 DIV using the MultiClamp 700B amplifier (Molecular Devices). The pipettes had resistance of 3-5 MΩ and were filled with the internal solution consisting of 115 mM CsCl, 10 mM HEPES, 2 mM $MgCl_2 \cdot 6H_2O$, 4 mM NaATP, 0.4 mM NaGTP, 0.5 mM EGTA, and pH was adjusted to 7.2-7.4 by CsOH. The neurons were perfused with the external solution of the following composition: 110 mM NaCl, 5 mM KCl, 2 mM $CaCl_2$, 0.8 mM $MgCl_2$, 10 mM HEPES, 10 mM Glucose, and pH was adjusted to 7.2-7.4 by NaOH. For miniature excitatory postsynaptic currents (mEPSCs) recording, tetrodotoxin (1 μM) and bicuculline (20 μM) were added into the external solution to block action potentials and the inhibitory current from GABA receptor, respectively. The signals were filtered at 2 kHz and sampled at 20 kHz using the Digidata 1440A (Molecular Devices). The holding potential was at −70 mV, and the recording lasted for 5 to 10 min. The data were analyzed by the commercial software MiniAnalysis (Synaptosoft).

Animal behavioral tests

Behavioral tests were performed in the chronological order of marble burying test, 3-chamber social interaction, home cage test, open field test, elevated plus maze test and olfactory habituation-dishabituation test.

Marble burying test: mice were placed into testing arena (40 cm length x 25 cm width x 18 cm height, bedding depth: 5 cm), each containing 20 glass marbles (laid out in four rows of five marbles equidistant from one another). After 30 minutes of exploration period, mice were carefully removed from the arena. A second experimenter blind to the genotypes of the tested mice scored the number and depth of the marbles. The marble burying score was arbitrarily defined as follow: 4 for completely buried marbles, 3 for marbles covered > 50% with bedding, 2 for marbles covered 50% with bedding, 1 for marbles covered < 50% with bedding, or 0 for anything less. The final marble burying score for each mouse was the sum of the scores of the 20 marbles. The score for each mouse was calculated in percentage as (final marble burying score) /80 (full score) x 100.

3-chamber social interaction: the test was performed in the 3-chamber arena. The size of the left, center and right chambers is 20 cm length x 40.5 cm width x 22 cm height (Bader et al., 2011). The chambers were separated by two clear plastic walls, each with a connecting doorway (10.2 cm width x 5.4 cm height). The test was divided into three stages. At stage 1, the testing mouse was placed into the central chamber for 5 minutes and the mouse was allowed to explore in the 3 chambers. At stage 2 (sociability), two identical cages (shape of a cup with evenly spaced metallic bars of diameter 7 cm) were each placed into the left and right chamber, and a stranger mouse of the same sex, similar age and size as the testing mouse was put inside the left cage. The testing mouse was allowed to explore the 3 chambers for 10 minutes. At stage 3 (social memory), the procedure was the same as stage 2 except another stranger mouse of the same sex, similar age and size as the testing mouse was put into the right cage. Approach behavior within 2 cm from targets was defined as interaction in term of sniffing time. All stages were video-recorded. The exploration time in each chamber was analyzed by ANY-maze tracking system. Sniffing was defined when the subject mouse is close to the cup and its nose is oriented to the cup (Yang et al., 2011; Leung et al., 2018).The sniffing time toward stranger mouse and inanimate cage (stage 2), as well as stranger mouse and familiar mouse (stage 3) was manually analyzed blind by a second experimenter.

Reciprocal social interaction in home cage: the test was performed in the arena (33 cm length x 12.5 cm width x 13 cm height, which was the same as the size of the home cage) with clean bedding. The day before the test, all testing mice were placed alone in separate cages. On the testing day, two testing mice of the same sex and genotype, similar age and size were put into the arena. The mice were allowed to explore and interact freely for 10 minutes. Number of events of various social behavior (follow, push-crawl, nose-nose sniffing, nose-anogenital sniffing) and non-social behavior (self-groom, jumping) were counted manually by a second experimenter who was blind to the genotypes of the mice.

Open field test: the test was performed in the square-based arena (40 cm length x 40 cm width x 40 cm height). The size of the center of arena is 20 cm length x 20 cm width. The testing mouse was allowed to explore freely in the arena for 10 minutes. The total distance traveled, exploration time and number of entries to the center were analyzed by ANY-maze tracking system.

Elevated plus maze test: the test was performed in an elevated plus-shaped maze, with horizontal close arms and vertical open arms connected by the central overlapping area. The size of each close arm is (30 cm length x 5 cm width) and is surrounded by opaque walls. The size of each open arm is (30 cm length x 5 cm width) without any wall to allow the testing mouse to see the elevated height. The testing mouse was allowed to explore freely in the maze for 5 minutes. The total distance traveled, time, and number of entries to the close arms and open arms were analyzed by ANY-maze tracking system.

Olfactory habituation-dishabituation test: 1 hour before the test, all testing mice were placed alone in separate clean cages. Non-social odors included water, almond (Dr. Oetker, 1: 200 diluted in water) and banana (Rayner's, 1: 1000 diluted in water). Social odors came from the bedding from two separated non-testing mouse cages which were not changed for 3 days. The five odors were delivered through cotton swabs. During the test, the testing mouse was allowed to sniff the fresh cotton swab that carried the same odor for 3 times, each with 2 minutes interval. In between each interval there was 1 minute resting time. The odors were performed in the chronological order of water, almond, banana, social odor 1 and social odor 2. The experiments were recorded, and the sniffing time during each interval, defined by the time the mouse nose in contact or directed toward the cotton swab, was calculated manually by a second experimenter who was blind to the mouse genotype.

QUANTIFICATION AND STATISTICAL ANALYSIS

Values presented in quantitative analysis were mean ± SEM and Shapiro-Wilk normality test was performed to each experimental group. For experimental group that passed the normality test, statistical analysis was performed by Student's t test when two experimental groups were analyzed or One-way ANOVA followed by Tukey post hoc test when more than two experimental groups were analyzed. For experimental group that did not pass the normality test, statistical analysis was performed by Mann-Whitney test when two experimental groups were analyzed or Kruskal-Wallis test followed by Dunn's multiple comparison test when more than two experimental groups were analyzed. For the olfactory habituation-dishabituation test, Two-way ANOVA followed by Tukey post hoc test was performed between the column factor (genotype) and row factor (odors). Statistical significance was defined as $p < 0.05$.